

# **A Class of Fluid-Structure Interaction Solvers with a Nearly Incompressible Elasticity Model**

**H. Yang**

**RICAM-Report 2012-02**

# A CLASS OF FLUID-STRUCTURE INTERACTION SOLVERS WITH A NEARLY INCOMPRESSIBLE ELASTICITY MODEL

HUIDONG YANG

ABSTRACT. In this paper, we present some numerical studies on two partitioned fluid-structure interaction solvers: a preconditioned GMRES solver and a Newton based solver, for the fluid-structure interaction problems employing a nearly incompressible elasticity model in a classical mixed displacement-pressure formulation. Both are highly relying on robust and efficient solvers for the fluid and structure sub-problems obtained from an extended and stabilized finite element discretization on hybrid meshes. For solving the discretized sub-problems with incompressible and nearly incompressible models, a special algebraic multigrid method capable of handling such general saddle point systems is investigated.

## 1. INTRODUCTION

The present work is an extension of our previous work [26, 22, 15, 23], where a Robin-Robin (RR) or a Robin-Neumann (RN) preconditioned GMRES solver (which is reinterpreted by introducing two Lagrange multipliers in the current work) and a partitioned Newton based solver have been applied to the interface equation of the fluid-structure interaction (FSI) problem discretized by the stabilized piecewise linear finite elements on hybrid meshes containing tetrahedral, hexahedral, prismatic and pyramidal elements. Both require robust and efficient sub-problem solutions obtained by applying special algebraic multigrid (AMG) methods, which are based on the work in [14, 20] and are extended in [22, 26] for general hybrid meshes.

As quite often considered by many others, e.g., in [7, 2, 3], a compressible linear elasticity model with a pure displacement formulation was used in our previous coupled FSI problem, which suffers from the so-called locking-effect (see [6, 4]) when the Poisson ratio  $\nu \rightarrow 0.5$ . Hence in the current work, we eliminate this nearly incompressible limitation in our structure model by using the mixed displacement-pressure formulation as in [10].

Since our FSI problem is discretized on general hybrid meshes, the stability of the sub-problems, e.g., the fluid problem, discretized by the extended piecewise linear finite elements on such meshes has been shown in [22]. It employs an enrichment of the velocity space with element-wise bubble functions, i.e. each nontetrahedral element adds as many bubble functions as the number of tetrahedral subdivisions

---

*Date:* January 16, 2012.

*2000 Mathematics Subject Classification.* 37M05, 65N30, 65N55, 74F10.

*Key words and phrases.* fluid-structure interaction, Robin-Robin/Robin-Neumann preconditioned GMRES, Newton based solver, algebraic multigrid methods, extended  $P_1$  element on hybrid meshes, mixed displacement/velocity-pressure formulation, nearly incompressible elasticity.

This work was supported by the Austrian Academy of Science.

on this element. The inf-sup condition on the discrete level was shown by explicitly constructing a so-called Fortin operator (see [6]). However this usually leads to an enlarged linear system. In this work, we follow a least-square stabilized finite element approach as suggested in [10], which overcomes the instability caused by equal-order finite element spaces for both displacement/velocity and pressure. Using Verfürth's trick [18], we explicitly show the stability on hybrid meshes for the mixed form with incompressible and nearly incompressible models. Moreover, we construct piecewise linear finite elements on a conforming subdivision of the original hybrid mesh without introducing any new node, which turns out to be more efficient than the previous introduced piecewise linear element on the hybrid mesh, see [24].

The performance of the sub-problem solvers is an important issue in the partitioned FSI algorithm, for which we use a special AMG method based on the work in [14]. A robust AMG solver for the saddle point problem arising from the fluid sub-problem discretized on pure tetrahedral meshes has been developed in [19, 20, 21], and was extended to such hybrid meshes in [22, 26], where a hierarchy of saddle point systems on all levels are constructed by using a stabilized coarsening strategy. This method is extended for solving a unified saddle point system arising from the discretized mixed displacement/velocity-pressure on the hybrid meshes. It turns out to be able to handle both incompressible and nearly incompressible models.

The remainder of this paper is organized in the following way. In Section 2, we set up a FSI problem. Section 3 deals with the RR (RN) coupled FSI system using two Lagrangian multipliers. Section 4 describes the partitioned Newton based FSI solver. In Section 5, two piecewise linear finite elements on hybrid meshes and their stabilized discretization for a general (nearly) incompressible model problem are shown. The stabilized coarsening strategy of the AMG solver for such saddle point problems on hybrid meshes are demonstrated in Section 6. Finally, in Section 7, a few numerical results are presented.

## 2. A FSI PROBLEM

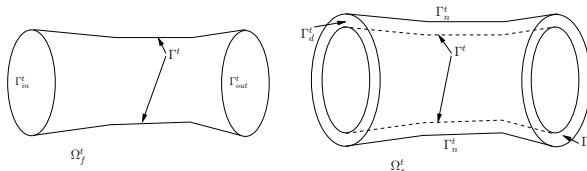


FIGURE 1. A schematic representation of a computational domain  $\Omega^t$ : fluid domain  $\Omega_f^t$  (left) and structure domain  $\Omega_s^t$  (right).

The computational fluid-structure domain  $\Omega^t \subset \mathbb{R}^3$  is decomposed into the deformable structure sub-domain  $\Omega_s^t$  and the fluid sub-domain  $\Omega_f^t$ :

$$\overline{\Omega^t} = \overline{\Omega_s^t} \cup \overline{\Omega_f^t},$$

where  $t$  denotes the time, and the subscripts  $s$  and  $f$  represent the structure and the fluid, respectively. The interface  $\Gamma^t$  is an intersection between boundaries of  $\Omega_s^t$  and  $\Omega_f^t$ :

$$\Gamma^t = \partial\Omega_s^t \cap \partial\Omega_f^t.$$

In addition,  $\Gamma_{in}^t$  and  $\Gamma_{out}^t$  denote the in-flow and out-flow boundaries of  $\Omega_f^t$ , respectively, and  $\Gamma_d^t$  and  $\Gamma_n^t$  denote the boundaries of  $\Omega_s^t$  with Dirichlet and Neumann boundary conditions, respectively. At  $t = 0$ , we have the initial (reference) configurations:  $\Omega_s^0, \Omega_f^0, \Gamma^0, \Gamma_{in}^0, \Gamma_{out}^0, \Gamma_d^0$  and  $\Gamma_n^0$ . See Fig. 1 for an illustration.

The evolution of the domain  $\Omega^t$  is obtained by two families of mappings:

$$\mathcal{L} : \Omega_s^0 \times (0, T) \rightarrow \Omega_s^t, (x_0, t) \mapsto x = \mathcal{L}(x_0, t) =: \mathcal{L}^t(x_0),$$

$$\mathcal{A} : \Omega_f^0 \times (0, T) \rightarrow \Omega_f^t, (x_0, t) \mapsto x = \mathcal{A}(x_0, t) =: \mathcal{A}^t(x_0),$$

for all  $x_0 \in \Omega_s^0$  and  $x_0 \in \Omega_f^0$ , respectively.

For the structure problem on the Lagrangian framework, the mapping  $\mathcal{L}^t$  is given by

$$\mathcal{L}^t(x_0) = x_0 + \hat{d}_s(x_0, t),$$

where  $\hat{d}_s(x_0, t)$  denotes the displacement of the structure domain at time  $t$ . For the fluid problem, an arbitrary Lagrangian-Eulerian (ALE) framework (see [9]) is used:

$$\mathcal{A}^t(x_0) = x_0 + \hat{d}_f(x_0, t),$$

where  $\hat{d}_f(x_0, t)$  denotes the displacement of the fluid domain at time  $t$ , and is typically defined as a harmonic extension  $\hat{d}_f = \text{Ext}(\hat{d}_s|_{\Gamma^0})$  of the structure displacement on  $\Gamma^0$ :

$$-\Delta \hat{d}_f = 0 \text{ in } \Omega_f^0, \hat{d}_f = 0 \text{ on } \Gamma_{in}^0 \cup \Gamma_{out}^0, \hat{d}_f = \hat{d}_s \text{ on } \Gamma^0.$$

We also introduce

$$\hat{w}_s := \partial_t \mathcal{L}^t = \partial_t \hat{d}_s \text{ and } \hat{w}_f := \partial_t \mathcal{A}^t = \partial_t \hat{d}_f$$

for the structure and fluid domain velocities, respectively.

For evaluating the time derivative of a function  $g$  on the moving domain  $\Omega_f^t$ , we define the ALE time derivative

$$\partial_t g|_{x_0} : \Omega_f^t \times (0, T) \rightarrow \mathbb{R},$$

$$\partial_t g|_{x_0}(x, t) = \partial_t (g \circ \mathcal{A}^t) \circ \mathcal{A}^{t-1}(x) = \frac{\partial g}{\partial t} + (w_f \cdot \nabla)g,$$

where  $w_f(x, t) = \hat{w}_f \circ \mathcal{A}^{t-1}$ .

Then the coupled system of the FSI problem in strong form reads: Find the fluid velocity  $u = u(x, t)$  and pressure  $p_f = p_f(x, t)$ , and the structure displacement  $\hat{d}_s = \hat{d}_s(x_0, t)$  and "pressure"  $\hat{p}_s = \hat{p}_s(x_0, t)$  such that (2.1) fulfills

$$(2.1a) \rho_f \partial_t u|_{x_0} + \rho_f ((u - w_f) \cdot \nabla)u - \nabla \cdot \sigma_f(u, p_f) = 0 \quad \text{in } \Omega_f^t \times (0, T),$$

$$(2.1b) \quad \nabla \cdot u = 0 \quad \text{in } \Omega_f^t \times (0, T),$$

$$(2.1c) \quad \sigma_f(u, p)n_f = g_{in}^t \quad \text{on } \Gamma_{in}^t,$$

$$(2.1d) \quad \sigma_f(u, p)n_f = 0 \quad \text{on } \Gamma_{out}^t,$$

$$(2.1e) \quad \rho_s \partial_t^2 \hat{d}_s - \nabla \cdot \hat{\sigma}_s(\hat{d}_s, \hat{p}_s) = 0 \quad \text{in } \Omega_s^0 \times (0, T),$$

$$(2.1f) \quad \nabla \cdot \hat{d}_s + \vartheta \hat{p}_s = 0 \quad \text{in } \Omega_s^0 \times (0, T),$$

$$(2.1g) \quad \hat{\sigma}_s(\hat{d}_s)\hat{n}_s = 0 \quad \text{on } \Gamma_n^0,$$

$$(2.1h) \quad \hat{d}_s = 0 \quad \text{on } \Gamma_d^0,$$

$$(2.1i) \quad u \circ \mathcal{A}^t = \partial_t \hat{d}_s \quad \text{on } \Gamma^0,$$

$$(2.1j) \quad \sigma_f(u, p)n_f \circ \mathcal{A}^t + \hat{\sigma}_s(\hat{d}_s)\hat{n}_s = 0 \quad \text{on } \Gamma^0,$$

and in addition

$$(2.2) \quad \Omega_f^t = \mathcal{A}^t(\Omega_f^0).$$

Here  $\rho_f$  and  $\rho_s$  denote the fluid and structure densities, respectively, and  $n_f$  and  $\hat{n}_s$  are the outward normals to  $\Omega_f^t$  and  $\Omega_s^0$ , respectively.

In particular the Cauchy stress tensor for the Newtonian and incompressible flow is given by

$$\sigma_f(u, p) = 2\mu\varepsilon(u) - p_f I,$$

where  $\mu$  is the fluid dynamic viscosity and

$$\varepsilon(u) = \frac{1}{2}(\nabla u + (\nabla u)^T)$$

the strain rate tensor. The Neumann boundary condition on  $\Gamma_{in}^t$  is given by a function  $g_{in}^t$ .

For the structure, the linear Saint Venant-Kirchhoff elastic model with the displacement-pressure formulation is used

$$\hat{\sigma}_s(\hat{d}_s) = 2\mu^l \varepsilon(\hat{d}_s) - 2\mu^l \hat{p}_s I.$$

Here

$$\begin{aligned} \varepsilon(\hat{d}_s) &= \frac{1}{2}(\nabla \hat{d}_s + (\nabla \hat{d}_s)^T), \\ \hat{p}_s &= -\frac{1}{\vartheta} \nabla \cdot \hat{d}_s, \quad \vartheta = \frac{1-2\nu}{\nu} \end{aligned}$$

and  $\mu^l$  is the shear modulus given by

$$\mu^l = \frac{E}{2(1+\nu)}$$

with the Young's modulus  $E$  and the Poisson ratio  $\nu$ .

For the fluid (2.1a) and (2.1b) state the momentum balance and mass conservation laws, respectively. For the structure, (2.1e) states the momentum balance law. A no-slip condition and an equilibrium of the surface traction on  $\Gamma^0$  are given by (2.1i) and (2.1j), respectively. The remaining conditions (2.1c), (2.1d), (2.1h) and (2.1g) are prescribed corresponding boundary conditions for the fluid and structure sub-problems. In addition, a geometrical problem (2.2) has to be solved at time  $t$ . It is easy to see that besides the nonlinearity from the convection part in (2.1a), the geometrical nonlinearity causes another difficulty for solving the coupled FSI problem. To complete the problem, the following initial conditions are prescribed:  $u(x_0, 0) = 0$ ,  $\hat{d}_s(x_0, 0) = 0$ ,  $\hat{w}_s(x_0, 0) = 0$ .

### 3. A RR (RN) COUPLED FSI SYSTEM

**3.1. Time discretization and linearization.** For the time discretization of the FSI system (2.1), we follow the strategy in [26, 7], where an implicit Euler scheme for the fluid and a first order Newmark method for the structure are used. The nonlinear convective term is treated in a semi-implicit way as in [8, 26]. The geometrical nonlinearity is handled by a first order extrapolation  $\Omega_f^t = \Omega_f^{t^n}$  for  $t \in [t^n, t^{n+1})$ , see e.g., [2], which is a fix point approach for handling the geometrical nonlinearity.

Let  $\Delta t$  be the time step size and  $t^n = n\Delta t$ ,  $n \in \{0, 1, \dots, N\}$  be the time level at  $n$ . Let  $z^n$  be an approximation of a function  $z$  for the time level  $t^n$ . The standard backward difference operator  $\delta_t(\cdot)$  is given by  $\delta_t z = (z - z^n)/\Delta t$ .

The time discretized system reads (for simplicity of notations, we do not include the boundary conditions): Given  $u^n$ ,  $\hat{d}_s^n$ ,  $\hat{w}_s^n$  and  $\Omega_f^{t^n}$ , find  $u^{n+1}$ ,  $p^{n+1}$ ,  $\hat{d}_s^{n+1}$ ,  $\hat{p}_s^{n+1}$  on the time level  $t^{n+1}$  such that (3.1) satisfies,

$$(3.1) \quad \begin{aligned} \rho_f \delta_t u^{n+1}|_{x_0} + \rho_f ((u^n - w_f^n) \cdot \nabla) u^{n+1} - \nabla \cdot \sigma_f(u^{n+1}, p^{n+1}) &= 0 && \text{in } \Omega_f^{t^n}, \\ \nabla \cdot u^{n+1} &= 0 && \text{in } \Omega_f^{t^n}, \\ \rho_s \delta_{tt} \hat{d}_s^{n+1} - \nabla \cdot \hat{\sigma}_s(\hat{d}_s^{n+1}, \hat{p}_s^{n+1}) &= 0 && \text{in } \Omega_s^0, \\ \nabla \cdot \hat{p}_s^{n+1} + \varepsilon \hat{p}_s &= 0 && \text{in } \Omega_s^0, \\ u^{n+1} \circ \mathcal{A}^{t^n} &= \delta_t \hat{d}_s^{n+1} && \text{on } \Gamma^0, \\ \sigma_f(u^{n+1}, p^{n+1}) n_f \circ \mathcal{A}^{t^n} + \hat{\sigma}_s(\hat{d}_s^{n+1}, \hat{p}_s^{n+1}) \hat{n}_s &= 0 && \text{on } \Gamma^0, \end{aligned}$$

where

$$\delta_t z^{n+1}|_{x_0} = (z^{n+1} - z^n) / \Delta t$$

is the backward difference for the ALE time derivative, and

$$\delta_{tt} \hat{d}_s^{n+1} = 2(\hat{d}_s^{n+1} - \hat{d}_s^n) / \Delta t^2 - 2\hat{w}_s^n / \Delta t.$$

The following updates are necessary for the next time level

$$\begin{aligned} \hat{d}_f^{n+1} &= \text{Ext}(\hat{d}_s^{n+1}|_{\Gamma^0}), \quad \Omega_f^{n+1} = \mathcal{A}^{t^{n+1}}(\Omega_f^0), \\ w_f^{n+1} &= \delta_t \hat{d}_f^{n+1} \circ \mathcal{A}^{t^{n+1}-1}, \quad \hat{w}_s^{n+1} = 2(\hat{d}_s^{n+1} - \hat{d}_s^n) - \hat{w}_s^n. \end{aligned}$$

**3.2. A RR (RN) system with Lagrangian multipliers.** Instead of imposing the continuity of velocities and fluxes (2.1i)-(2.1j) from the fluid and structure sides on the interface, we use the RR transmission conditions for  $t \in [t^n, t^{n+1})$ :

$$(3.2) \quad \begin{aligned} \alpha_f u \circ \mathcal{A}^t + \sigma_f(u, p) n_f \circ \mathcal{A}^t &= \alpha_f \delta_t \hat{d}_s - \hat{\sigma}_s(\hat{d}_s, \hat{p}_s) \hat{n}_s, \\ \alpha_s \delta_t \hat{d}_s + \hat{\sigma}_s(\hat{d}_s, \hat{p}_s) \hat{n}_s &= \alpha_s u \circ \mathcal{A}^t - \sigma_f(u, p) n_f \circ \mathcal{A}^t \end{aligned}$$

on  $\Gamma^0$ , with weighting parameters  $\alpha_f > 0$  and  $\alpha_s > 0$ .

**Remark 1.** For a limiting case  $\alpha_s = 0$ , we obtain the RN interface condition, which is used in our numerical experiments. However, without loss of generality, we form the interface conditions by the RR equations.

It is easy to see that these two interface conditions are equivalent to the original two. In [2], they are proposed in an iterative setting for the FSI problem with a pure displacement structure model. In [23], we did a detailed numerical study on the RN preconditioned GMRES solver for the FSI problem using the algebraic multigrid accelerations on hybrid meshes.

Here we reinterpret the algorithm by introducing two Lagrangian multipliers

$$\lambda_f := \sigma_f(u, p) n_f \circ \mathcal{A}^t \text{ and } \lambda_s := \hat{\sigma}_s(\hat{d}_s, \hat{p}_s) \hat{n}_s$$

for the surface traction on the interface from the fluid and the structure sides, respectively, which are corresponding dual variables.

Then the linearized coupled system of (2.1) at each time step (after the extended linear finite element discretization on hybrid meshes, see Section 5) with the RR

transmission conditions (3.2) on the interface is given by (3.3).

$$(3.3) \quad \begin{pmatrix} Y_{ff} & Y_{f\Gamma} & 0 & 0 & 0 & 0 \\ Y_{\Gamma f} & Y_{\Gamma\Gamma} & 0 & 0 & -M_\Gamma & 0 \\ 0 & 0 & X_{\Gamma\Gamma} & X_{\Gamma s} & 0 & -M_\Gamma \\ 0 & 0 & X_{s\Gamma} & X_{ss} & 0 & 0 \\ 0 & \alpha_f M_\Gamma & -\frac{\alpha_f}{\Delta t} M_\Gamma & 0 & M_\Gamma & M_\Gamma \\ 0 & -\alpha_s M_\Gamma & \frac{\alpha_s}{\Delta t} M_\Gamma & 0 & M_\Gamma & M_\Gamma \end{pmatrix} \begin{pmatrix} V_f \\ V_\Gamma \\ D_\Gamma \\ D_s \\ \Lambda_f \\ \Lambda_s \end{pmatrix} = \begin{pmatrix} F_f \\ F_{f\Gamma} \\ F_{s\Gamma} \\ F_s \\ -\frac{\alpha_f}{\Delta t} M_\Gamma D_\Gamma^n \\ \frac{\alpha_s}{\Delta t} M_\Gamma D_\Gamma^n \end{pmatrix}.$$

Here  $V_\Gamma$  and  $D_\Gamma$  represent the nodal degrees of freedom of the fluid velocity and the structure displacement associated to the interface nodes, respectively.  $V_f^T = (V_p^T, V_v^T)$  with  $V_p$  representing all the fluid pressure nodal degrees of freedom and  $V_v$  the remaining velocity nodal degrees of freedom.  $D_s^T = (D_p^T, D_d^T)$  with  $D_p^T$  representing all the hydrostatic pressure nodal degrees of freedom and  $D_d^T$  the remaining structure displacement nodal degrees of freedom.  $\Lambda_f$  and  $\Lambda_s$  correspond to the nodal degrees of freedom of the surface traction  $\lambda_f$  and  $\lambda_s$ , respectively. The stiffness matrices

$$\begin{pmatrix} Y_{ff} & Y_{f\Gamma} \\ Y_{\Gamma f} & Y_{\Gamma\Gamma} \end{pmatrix} \text{ and } \begin{pmatrix} X_{\Gamma\Gamma} & X_{\Gamma s} \\ X_{s\Gamma} & X_{ss} \end{pmatrix}$$

on the left hand side result from the extended finite element discretization of the fluid and structure sub-problems with homogeneous Neumann boundary conditions on the interface.  $M_\Gamma$  is the mass matrix on the interface. The vectors on the right hand side arise from the finite element assembly of the body forces, the Neumann boundary conditions, and the structure displacement at the previous time step level  $t^n$ . For more details, see [23].

**Remark 2.** We also note that from the last two equations in (3.3), when  $\alpha_f \neq \alpha_s$ , it follows that

$$\Lambda_f = -\Lambda_s \text{ and } V_\Gamma = \frac{1}{\Delta t}(D_\Gamma - D_\Gamma^n).$$

Then an elimination of  $\Lambda_f$  and  $\Lambda_s$  in (3.3) leads to the following linear system of the coupled problem (2.1):

$$(3.4) \quad \begin{pmatrix} Y_{ff} & Y_{f\Gamma} & 0 & 0 \\ Y_{\Gamma f} & Y_{\Gamma\Gamma} & X_{\Gamma\Gamma} & X_{\Gamma s} \\ 0 & 0 & X_{s\Gamma} & X_{ss} \\ 0 & M_\Gamma & -\frac{1}{\Delta t} M_\Gamma & 0 \end{pmatrix} \begin{pmatrix} V_f \\ V_\Gamma \\ D_\Gamma \\ D_s \end{pmatrix} = \begin{pmatrix} F_f \\ F_\Gamma \\ F_s \\ -\frac{1}{\Delta t} M_\Gamma D_\Gamma^n \end{pmatrix}$$

with  $F_\Gamma = F_{f\Gamma} + F_{s\Gamma}$ .

**3.3. A RR (RN) iteration of the FSI system.** It is obvious to see that in (3.3) the fluid and structure sub-problems are coupled by the interface nodal degrees of freedom  $V_\Gamma$ ,  $D_\Gamma$ ,  $\Lambda_f$  and  $\Lambda_s$ . For any given  $D_\Gamma$  and  $\Lambda_s$  (or  $V_\Gamma$  and  $\Lambda_f$ ), the coupled system (3.3) is decoupled into the fluid and structure sub-problems.

Providing  $D_\Gamma^k$  and  $\Lambda_s^k$  at the iteration step  $k \geq 0$  in (3.3), then from the fifth equation in (3.3), it follows

$$\Lambda_f^k = \frac{\alpha_f}{\Delta t}(D_\Gamma^n - D_\Gamma^k) + \Lambda_s^k - \alpha_f V_\Gamma^k.$$

Now the following fluid sub-problem (3.5) is completely decoupled from the structure sub-problem.

$$(3.5) \quad \begin{pmatrix} Y_{ff} & Y_{f\Gamma} \\ Y_{\Gamma f} & Y_{\Gamma\Gamma} + \alpha_f M_\Gamma \end{pmatrix} \begin{pmatrix} V_f^k \\ V_\Gamma^k \end{pmatrix} = \begin{pmatrix} F_f \\ F_{f\Gamma} - \frac{\alpha_f}{\Delta t} M_\Gamma (D_\Gamma^n - D_\Gamma^k) - M_\Gamma \Lambda_s^k \end{pmatrix}.$$

Providing  $V_\Gamma^k$  and  $\Lambda_f^k$ , from the sixth equation in (3.3), it follows

$$\Lambda_s^{k+1} = -\frac{\alpha_s}{\Delta t} (D_\Gamma - D_\Gamma^n) + \alpha_s V_\Gamma^k - \Lambda_f^k.$$

Then the following structure sub-problem (3.6) is completely decoupled from the fluid sub-problem.

$$(3.6) \quad \begin{pmatrix} X_{\Gamma\Gamma} + \frac{\alpha_s}{\Delta t} M_\Gamma & X_{\Gamma s} \\ X_{s\Gamma} & X_{ss} \end{pmatrix} \begin{pmatrix} D_\Gamma^{k+1} \\ D_s^{k+1} \end{pmatrix} = \begin{pmatrix} F_{s\Gamma} + \frac{\alpha_s}{\Delta t} M_\Gamma D_\Gamma^n + \alpha_s M_\Gamma V_\Gamma^k - M_\Gamma \Lambda_f^k \\ F_s \end{pmatrix}.$$

Note that  $M_\Gamma \Lambda_f^k$  and  $M_\Gamma \Lambda_s^k$  are evaluated as the residual of the momentum equations in weak forms from the fluid and the structure sub-problems, respectively.

**Remark 3.** We remark that the above RR iterations are corresponding to the RR iterations in [3], which are based on a reduced coupled system (using the structure velocity variables on the interface) similar to (3.4), without using the Lagrangian multipliers. In case  $\alpha_f > 0$ ,  $\alpha_s = 0$ , the above RR iterations are reduced to the RN iterations.

The Schur complement equation for (3.4) reads:

$$(3.7) \quad \mathcal{S}_\Gamma D_\Gamma = H_\Gamma,$$

where

$$\mathcal{S}_\Gamma = \frac{1}{\Delta t} Y_{\Gamma\Gamma} - \frac{1}{\Delta t} Y_{\Gamma f} Y_{ff}^{-1} Y_{f\Gamma} + X_{\Gamma\Gamma} - X_{\Gamma s} X_{ss}^{-1} X_{s\Gamma},$$

and the right hand side is given by

$$(3.8) \quad H_\Gamma = F_\Gamma - Y_{\Gamma f} Y_{ff}^{-1} (F_f + \frac{1}{\Delta t} Y_{f\Gamma} D_\Gamma^n) + \frac{1}{\Delta t} Y_{\Gamma\Gamma} D_\Gamma^n - X_{\Gamma s} X_{ss}^{-1} F_s.$$

**Remark 4.** For the special case  $\alpha_f > 0$ ,  $\alpha_s = 0$ , the above RN iteration is nothing but a preconditioned Richardson iteration applied to the Schur complement equation (3.7):

$$(3.9) \quad D_\Gamma^{k+1} = D_\Gamma^k + P_\Gamma^{-1} (H_\Gamma - \mathcal{S}_\Gamma D_\Gamma^k),$$

with the preconditioner  $P_\Gamma$

$$(3.10) \quad P_\Gamma = \left( \frac{\Delta t}{\alpha_f} \tilde{Y}_\Gamma + M_\Gamma \right) M_\Gamma^{-1},$$

where  $\tilde{Y}_\Gamma = \frac{1}{\Delta t} Y_{\Gamma f} Y_{ff}^{-1} Y_{f\Gamma}$ .

**Remark 5.** In case  $\alpha_f \rightarrow +\infty$ ,  $P_\Gamma \approx I$ , it corresponds to a Dirichlet-Neumann iteration, and an almost identity preconditioner. Thus this choice turns out to be very slow. In case  $\alpha_f \rightarrow 0$ ,  $P_\Gamma = \frac{\alpha_f}{\Delta t} \tilde{Y}_\Gamma M_\Gamma^{-1}$ , we obtain a Neumann-Neumann iteration. The detailed numerical comparison of these iterations for the FSI problem with a pure displacement structure model was reported in [23].

For the acceleration with the GMRES method (see [17]) applied to the RN preconditioned system (3.9), we refer to [23] and the reference therein.

#### 4. A PARTITIONED NEWTON BASED FSI SOLVER

The original partitioned Newton solver for the FSI problem with a pure displacement formulation was introduced in the work of [7, 8]. In [22, 25, 26], the Newton based FSI solver has been applied to the FSI problems on hybrid meshes, where the convection part is treated in convective form. In [23], detailed numerical comparisons of the preconditioned RN GMRES solver and the Newton based solver for the FSI problems on hybrid meshes were studied based on the pure displacement structure model.

For simplicity of presentation, we preserve some of the notations from Section 3. However, these are in general corresponding nonlinear operators (Steklov-Poincaré operators) in the setting of the Newton based FSI solver due to the geometrical and the material nonlinearities.

As (3.7) states, the original coupled problem (3.4) is reduced to a nonlinear equilibrium of the surface traction from the fluid and structure sides on the interface:

$$(4.1) \quad (\mathcal{S}_{f\Gamma} + \mathcal{S}_{s\Gamma})(D_\Gamma) = 0,$$

where

$$\mathcal{S}_{f\Gamma}(\cdot) = F_{f\Gamma} - Y_{\Gamma f} Y_{ff}^{-1} (F_f + \frac{1}{\Delta t} Y_{f\Gamma} D_\Gamma^n) + \frac{1}{\Delta t} Y_{\Gamma\Gamma} D_\Gamma^n + \underbrace{\frac{1}{\Delta t} (Y_{\Gamma\Gamma} - Y_{\Gamma f} Y_{ff}^{-1} Y_{f\Gamma})}_{:=\tilde{\mathcal{S}}_{f\Gamma}}(\cdot)$$

and

$$\mathcal{S}_{s\Gamma}(\cdot) = F_{s\Gamma} - X_{\Gamma s} X_{ss}^{-1} F_s - \underbrace{(X_{\Gamma\Gamma} - X_{\Gamma s} X_{ss}^{-1} X_{s\Gamma})}_{:=\tilde{\mathcal{S}}_{s\Gamma}}(\cdot)$$

represent Dirichlet-to-Neumann mappings for the fluid and the structure sub-problems, respectively.

A Newton iteration applied to the interface equation (4.1) is given in short: For  $k \geq 0$ ,

$$(4.2) \quad D_\Gamma^{k+1} = D_\Gamma^k + \left( \tilde{\mathcal{S}}'_{f\Gamma} + \tilde{\mathcal{S}}'_{s\Gamma} \right)^{-1} \mathcal{R}(D_\Gamma^k),$$

where

$$\mathcal{R}(D_\Gamma^k) = -\mathcal{S}_{f\Gamma}(D_\Gamma^k) - \mathcal{S}_{s\Gamma}(D_\Gamma^k).$$

Here the inverse of Jacobians might be evaluated by applying a preconditioned GMRES solver to the following

$$\left( \tilde{\mathcal{S}}'_{s\Gamma} \right)^{-1} \left( \tilde{\mathcal{S}}'_{f\Gamma} + \tilde{\mathcal{S}}'_{s\Gamma} \right) (\delta D_\Gamma^k) = \left( \tilde{\mathcal{S}}'_{s\Gamma} \right)^{-1} \mathcal{R}(D_\Gamma^k).$$

Note that, for the implementation, these matrices are not constructed explicitly, and their (inverse) applications to vectors correspond to Dirichlet-to-Neumann (Neumann-to-Dirichlet) mappings by solving the fluid and the structure sub-problems with prescribed Dirichlet (Neumann) conditions on the interface, respectively.

#### 5. WEAK FORMULATIONS AND THE FINITE ELEMENT DISCRETIZATION ON A HYBRID MESH

**5.1. Function spaces.** Let  $H^1(\Omega_s^0)$ ,  $L^2(\Omega_s^0)$ ,  $H^1(\Omega_f^0)$  and  $L^2(\Omega_f^0)$  denote the standard Sobolev and Lebesgue spaces (see [1]) on  $\Omega_s^0$  and  $\Omega_f^0$ , respectively.

For the fluid, the function spaces for the velocity and pressure are respectively given by

$$\begin{aligned} V_f^t &= \{v_f | v_f \circ \mathcal{A}^t = \hat{v}_f, \hat{v}_f \in [H^1(\Omega_f^0)]^3\}, \\ Q_f^t &= \{q_f | q_f \circ \mathcal{A}^t = \hat{q}_f, \hat{q}_f \in L^2(\Omega_f^0)\}. \end{aligned}$$

For the structure, we define

$$\begin{aligned} \hat{V}_s &= [H^1(\Omega_s^0)]^3, \quad \hat{V}_{s,0} = \{\hat{v}_s \in \hat{V}_s | \hat{v}_s = 0 \text{ on } \Gamma_d^0\} \\ \hat{Q}_s &= L^2(\Omega_s^0). \end{aligned}$$

5.1.1. *The weak formulation of the time discretized fluid problem.* By the standard technique applied to the time discretized fluid sub-problem in (3.1), we obtain the following mixed variational problem: Find  $(u^{n+1}, p_f^{n+1}) \in V_f^{t^{n+1}} \times Q_f^{t^{n+1}}$  such that

$$(5.1a) \quad a_f(u^{n+1}, v_f) + b_f(v_f, p_f^{n+1}) = \langle F_f^n, v_f \rangle,$$

$$(5.1b) \quad b_f(u^{n+1}, q_f) = 0$$

for all  $(v_f, q_f) \in V_f^{t^{n+1}} \times Q_f^{t^{n+1}}$ , with the bilinear and linear forms

$$\begin{aligned} a_f(u, v_f) &= \frac{\rho_f}{\Delta t} (u, v_f)_{\Omega_f^{t^n}} + \rho_f ((u^n - w_f^n) \cdot \nabla) u, v_f)_{\Omega_f^{t^n}} \\ &\quad + \mu (\varepsilon(u), \nabla v_f)_{\Omega_f^{t^n}}, \end{aligned}$$

$$b_f(v_f, q_f) = -(\nabla \cdot v_f, q_f)_{\Omega_f^{t^n}},$$

$$\langle F_f^n, v_f \rangle = \frac{\rho_f}{\Delta t} (u^n, v_f)_{\Omega_f^{t^n}} + \langle g_{in}, v_f \rangle_{\Gamma_{in}^{t^n}},$$

where  $(\cdot, \cdot)_{\Omega_f^{t^n}}$  denotes the product in  $L^2(\Omega_f^{t^n}) \times L^2(\Omega_f^{t^n})$ , and  $\langle \cdot, \cdot \rangle_{\Gamma_{in}^{t^n}}$  the duality product in  $H^{1/2}(\Gamma^{t^n}) \times H^{-1/2}(\Gamma^{t^n})$ . Here  $H^{1/2}(\Gamma^{t^n})$  denotes the Sobolev space of the trace on  $\Gamma^{t^n}$  of functions from  $V_f^{t^{n+1}}$ , and  $H^{-1/2}(\Gamma^{t^n})$  its dual.

5.1.2. *The weak formulation of the time discretized structure problem.* The weak formulation for the structure sub-problem in (3.1) reads: Find  $(\hat{d}_s^{n+1}, \hat{p}_s^{n+1}) \in \hat{V}_{s,0} \times \hat{Q}_s$  such that

$$(5.2a) \quad a_s(\hat{d}_s^{n+1}, \hat{v}_s) + b_s(\hat{v}_s, \hat{p}_s^{n+1}) = \langle F_s^n, \hat{v}_s \rangle,$$

$$(5.2b) \quad b_s(\hat{d}_s^{n+1}, \hat{q}_s) - c_s(\hat{p}_s^{n+1}, \hat{q}_s) = 0$$

for all  $(\hat{v}_s, \hat{q}_s) \in \hat{V}_{s,0} \times \hat{Q}_s$ , with the bilinear and linear forms

$$a_s(\hat{d}_s, \hat{v}_s) = \frac{2\rho_s}{\Delta t^2} (\hat{d}_s, \hat{v}_s)_{\Omega_s^0} + \mu^l (\varepsilon(\hat{d}_s), \nabla \hat{v}_s)_{\Omega_s^0},$$

$$b_s(\hat{v}_s, \hat{q}_s) = -2\mu^l (\nabla \cdot \hat{v}_s, \hat{q}_s)_{\Omega_s^0},$$

$$c_s(\hat{p}_s, \hat{q}_s) = 2\mu^l \vartheta(\hat{p}_s, \hat{q}_s)_{\Omega_s^0},$$

$$\langle \hat{F}_s^n, \hat{v}_s \rangle = \frac{2\rho_s}{\Delta t} (\hat{d}_s^n + \Delta t \hat{w}_s^n, \hat{v}_s)_{\Omega_s^0},$$

where  $(\cdot, \cdot)_{\Omega_s^0}$  denotes the product in  $L^2(\Omega_s^0) \times L^2(\Omega_s^0)$ .

Note that on the interface we impose a conformity of traces of functions from the fluid velocity and structure displacement spaces, i.e., for  $v_f \in V_f^t$  and  $\hat{v}_s \in \hat{V}_{s,0}$ ,

$$v_f \circ \mathcal{A}^t = \hat{v}_s \text{ on } \Gamma^0.$$

**Remark 6.** For solvability of the systems (5.1) and (5.2), the boundary conditions (Dirichlet, Neumann, or Robin) on the interface for the fluid and the structure sub-problems have to be included into the finite element spaces or into the weak form. For details we refer to [23].

**5.2. Piecewise linear finite elements on a hybrid mesh.** The spatial discretization was done by a finite element method on the hybrid mesh composed of four types of elements: tetrahedron, pyramid, prism and hexahedron (see Fig. 2). Let  $\mathcal{M}_h$  be an admissible triangulation of a computational domain  $\Omega$  into hybrid elements, i.e. any two elements from  $\mathcal{M}_h$  either have no intersection, or have a common node, or have a common edge, or have a common face.

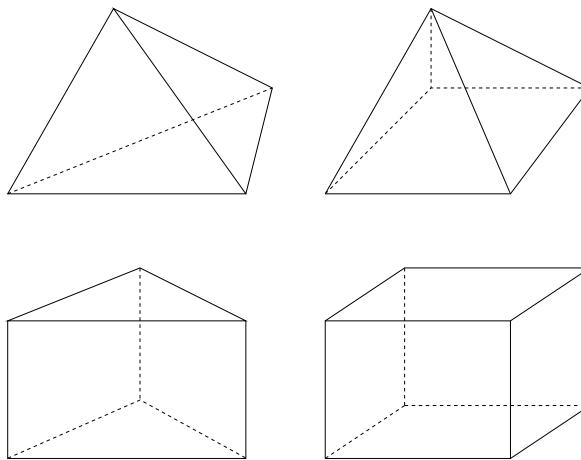


FIGURE 2. Hybrid elements

In [24], two piecewise linear finite elements on such hybrid meshes are constructed and applied to the FSI problem with a pure displacement structure formulation. These two elements are constructed in the following, and are applicable to both sub-problems in mixed displacement/velocity-pressure formulations.

**5.2.1. Piecewise linear elements on a conforming subdivision of a hybrid mesh without additional nodes (Fem-I).** The first finite element is a standard  $P_1$  element constructed on the conforming subdivision of pyramids, prisms and hexahedra into pure tetrahedra without introducing any new node. This procedure is performed in the following two steps.

First, let nodal global numbering be an identifier of each node. We split each quadrilateral face into two triangles by connecting the diagonal including the node with the smallest global numbering from the four nodes on this face, which keeps the subdivision conforming across element faces.

Second, we verify that further subdivisions of pyramids, prisms and hexahedra into tetrahedra only require proper local nodal connections inside each element. So no new nodes are added during this step.

By this means, a pyramid has two subdivision possibilities, see Table 1.

For a prism, we have two subdivision possibilities, see Table 2.

For a hexahedron, eight subdivision possibilities exist, see Table 3.

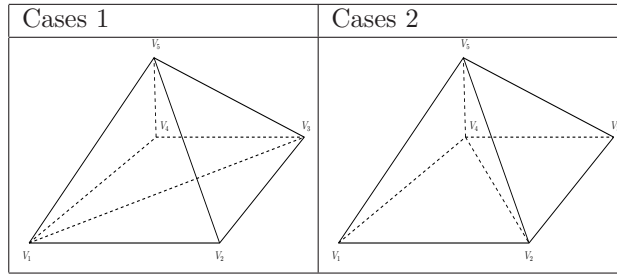


TABLE 1. Subdivisions of a pyramid.

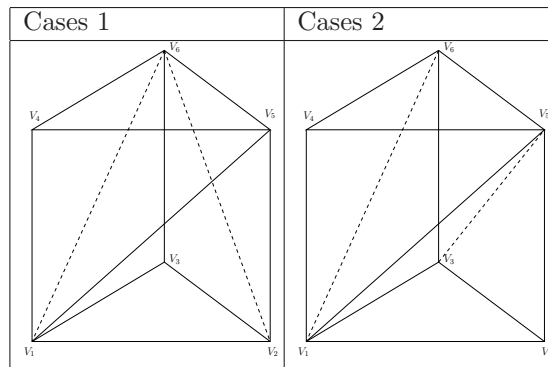


TABLE 2. Subdivisions of a prism.

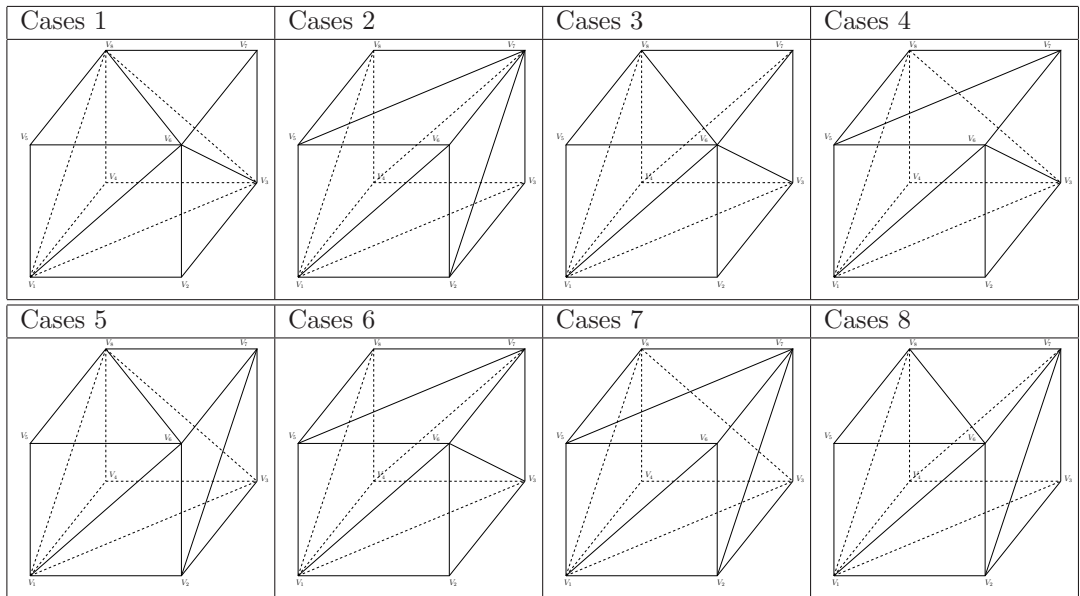


TABLE 3. Subdivisions of a hexahedron.

It is easy to see the piecewise linear finite element on such a hybrid mesh is nothing but the standard  $P_1$  element on the conforming subdivision of the original hybrid mesh without introducing any new degrees of freedom.

5.2.2. *An extended linear element on a hybrid mesh with additional nodes (Fem-II).*

The second finite element is an extended linear element on hybrid meshes. For this we first make a conforming subdivision of pyramids, prisms and hexahedra into pure tetrahedra by splitting each quadrilateral face into four triangles with added quadrilateral face center node, and then in each non-tetrahedral element connecting the original nodes and the new face center nodes with its added volume center node.

By this means, a pyramid is split into eight tetrahedra, a prism into fourteen tetrahedra and a hexahedra into twenty-four tetrahedra, see Fig. 3 for an illustration.

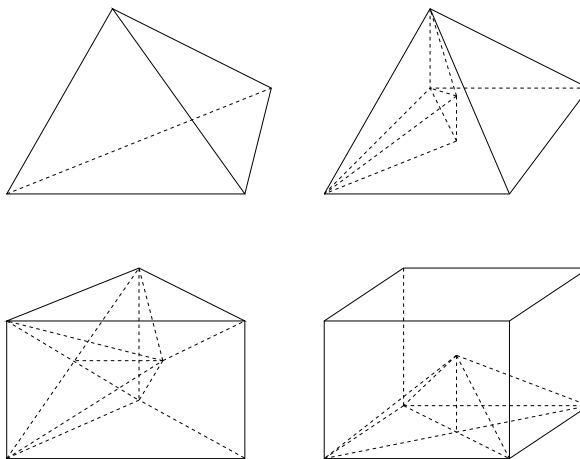


FIGURE 3. Splitting of hybrid elements into tetrahedra with added nodes.

One easily sees that such a subdivision results in an admissible refinement of the original hybrid mesh  $\mathcal{M}_h$ . So it leads to a conforming mesh with additional nodes, i.e. introducing new nodal degrees of freedom.

Then we take the standard  $P_1$  finite element on the tetrahedral subdivision and substitute the nodal degrees of freedom associated to the added nodes by averaging over neighbouring nodes of the original hybrid mesh. Each resulting nodal basis function turns out to be a weighted linear combination of the standard  $P_1$  basis functions on the subdivision, with larger support.

For constructing the extended linear element on  $\mathcal{M}_h$ , we firstly consider a nodal basis function on an element  $M$  from  $\mathcal{M}_h$  as follows: Let  $x$  be a node of  $M$ , let  $x_{F_i}$ ,  $i = 1, \dots$ , denote the center node of those non-triangular faces  $F_i$  which contain  $x$  as a node, and let  $x_M$  denote the center node of  $M$ .

Then on the element  $M$ , the nodal basis function  $\varphi$  associated with the node  $x$  is given by

$$(5.3) \quad \varphi = \tilde{\varphi} + \sum_i \frac{1}{N_{F_i}} \tilde{\varphi}_{F_i} + \frac{1}{N_M} \tilde{\varphi}_M ,$$

where  $\tilde{\varphi}$ ,  $\tilde{\varphi}_{F_i}$ , and  $\tilde{\varphi}_M$  denote the nodal basis functions of the  $P_1$  element on the subdivision of  $M$  associated with the nodes  $x$ ,  $x_{F_i}$  and  $x_M$ , respectively, and  $N_{F_i}$  and  $N_M$  are the numbers of nodes of the face  $F_i$  and the element  $M$ , respectively. It is easy to see that such a constructed piece-wise linear basis function preserve the partition of unity, and has larger support compared to a standard linear basis function.

Then the finite element space of the extended linear element on  $\mathcal{M}_h$  is constructed by a span of the local basis functions on each element  $M$ , i.e.,

$$(5.4) \quad \tilde{V}_h = \{v \in C(\bar{\Omega}) : v|_M \in \Phi_M, \forall M \in \mathcal{M}_h\},$$

where

$$\Phi_M = \text{span}\{\varphi : M \in \mathcal{M}_h\}.$$

**Remark 7.** *The first finite element method might be seen as a special case of the second one, where all elements are tetrahedron. Thus in the following, we only prove the stability of the second finite element method, which covers the first one as well.*

**Remark 8.** *Compared with the first finite element method, the second one is more expensive since it produces much more tetrahedra and the extended linear basis function has much larger support. Thus in computation, the first finite element method will be faster than the second one due to the less costly finite element assembly procedure. However, for hybrid meshes containing arbitrary types of polyhedral elements, the second finite element method might be easier to adapt. Their performance comparison for the FSI problem with pure displacement structure formulation has been reported in [24].*

5.2.3. *Stability.* We firstly introduce some useful notations:  $x_i$ , the vertices of an element  $M \in \mathcal{M}_h$ , where  $i \in \{1, \dots, n_V\}$  with  $n_V$  the number of vertices of  $M$ ;  $\varphi_i$ , the extended linear basis function associated with the vertex  $x_i$  on  $M$ ;  $\mathcal{P}_i$ , the patch of all elements from  $\mathcal{M}_h$  containing  $x_i$  as a vertex;  $\mathcal{P} = \bigcup \mathcal{P}_i$ , the union of all the patches  $\mathcal{P}_i$  covering an element  $M \in \mathcal{M}_h$ ;  $h_T$ , the diameter of the element  $T \in \mathcal{T}_h$ ;  $h_M$ , the diameter of the element  $M \in \mathcal{M}_h$ ;  $h = \sup_{T \in \mathcal{T}_h} \{h_T\}$ , the supremum of  $h_T$  over all  $T \in \mathcal{T}_h$ ;  $\rho_T$ , the diameter of the inscribed ball in  $T \in \mathcal{T}_h$ . See Fig. 4 for an illustration.

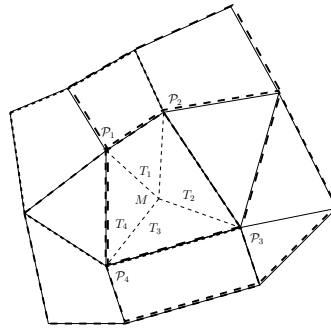


FIGURE 4. The patch  $\mathcal{P} = \bigcup \mathcal{P}_i$ ,  $i \in \{1, \dots, 4\}$  covers the element  $M$ . The element  $M$  is split into four triangular (tetrahedral) elements  $T_i$ ,  $i \in \{1, \dots, 4\}$ .

**Assumption 9.** We assume that  $\mathcal{T}_h$  is regular, i.e. there exists a positive constant  $\sigma$  such that for all  $T \in \mathcal{T}_h$ ,

$$(5.5) \quad h_T / \rho_T \leq \sigma$$

The local projection  $\pi_i : L^2(\mathcal{P}_i) \rightarrow \mathbb{R}$  is given by

$$(5.6) \quad \pi_i v = \frac{1}{|\mathcal{P}_i|} \int_{\mathcal{P}_i} v dx,$$

where  $|\mathcal{P}_i|$  is the volume of the patch  $\mathcal{P}_i$ . Using the value prescribed by (5.6) as nodal value at  $x_i$ , the Clément interpolation operator  $I_M$  on a element  $M$  is defined by

$$(5.7) \quad I_M v = \sum_{i=1}^{n_V} (\pi_i v) \varphi_i = \sum_{i=1}^{n_V} \frac{\varphi_i}{|\mathcal{P}_i|} \int_{\mathcal{P}_i} v dx.$$

Under regular mesh assumptions, we have

**Lemma 10.** If  $v \in H^1(\mathcal{P}_i)$ , then

$$\begin{aligned} \|v - \pi_i v\|_{L^2(\mathcal{P}_i)} &\leq 2\|v\|_{L^2(\mathcal{P}_i)}, \\ \|v - \pi_i v\|_{L^2(\mathcal{P}_i)} &\leq ch_{\mathcal{P}_i} |v|_{H^1(\mathcal{P}_i)}, \\ |v - \pi_i v|_{H^1(\mathcal{P}_i)} &= |v|_{H^1(\mathcal{P}_i)}, \end{aligned}$$

where  $c$  is a positive and mesh independent parameter and  $h_{\mathcal{P}_i} = \sup_{T \in \mathcal{P}_i} \{h_T\}$ .

Correspondingly, we have the following error estimates.

**Lemma 11.** If  $v \in H^1(\mathcal{P})$ , then

$$\begin{aligned} \|v - I_M v\|_{L^2(M)} &\leq c\|v\|_{L^2(\mathcal{P})}, \\ \|v - I_M v\|_{L^2(M)} &\leq ch_{\mathcal{P}} |v|_{H^1(\mathcal{P})}, \\ |v - I_M v|_{H^1(M)} &\leq c|v|_{H^1(\mathcal{P})}, \end{aligned}$$

where  $c$  is a positive and mesh independent parameter and  $h_{\mathcal{P}} = \sup_{T \in \mathcal{P}} \{h_T\}$ .

We then define the global Clément operator  $I_C$  by

$$(5.8) \quad I_C|_M = I_M$$

for all  $M \in \mathcal{M}_h$ . It is easy to see that we have the following global error estimates.

**Theorem 12.** If  $v \in H^1(\Omega)$ , then

$$\begin{aligned} \|v - I_C v\|_{L^2(\Omega)} &\leq c\|v\|_{L^2(\Omega)}, \\ \|v - I_C v\|_{L^2(\Omega)} &\leq ch |v|_{H^1(\Omega)}, \\ |v - I_C v|_{H^1(\Omega)} &\leq c|v|_{H^1(\Omega)}, \end{aligned}$$

where  $c$  is a positive and mesh independent parameter.

For  $v \in H^2(\Omega)$ , we define a Lagrange interpolation operator  $I_L : H^2(\Omega) \rightarrow V_h^H$  element-wise by

$$I_L v|_M = \sum_{i=1}^{n_V} v(x_i) \varphi_i$$

for all  $M \in \mathcal{M}_h$ .

Then we obtain

**Lemma 13.** For  $v \in H^2(M)$ , there exists a positive and mesh independent constant  $c$  such that

$$\begin{aligned} \|v - I_L v\|_{L^2(M)} &\leq ch_M^2 |v|_{H^1(M)}, \\ |v - I_L v|_{H^1(M)} &\leq ch_M |v|_{H^2(M)} \end{aligned}$$

for each  $M \in \mathcal{M}_h$ .

Correspondingly, we have the following global error estimates:

**Theorem 14.** For  $v \in H^2(\Omega)$ , there exists a positive and mesh independent constant  $c$  such that

$$(5.9) \quad \|v - I_L v\|_{L^2(\Omega)} \leq ch^2 |v|_{H^2(\Omega)},$$

$$(5.10) \quad |v - I_L v|_{H^1(\Omega)} \leq ch |v|_{H^2(\Omega)}.$$

For the proof of the above Lemmas and theorems, we refer to [22] for details.

**5.3. The stabilized lowest order displacement/velocity-pressure formulation.** As is well known, the equal-order interpolation for the displacement/velocity and the pressure leads to a violation of the inf-sup condition for the mixed formulations of the fluid and the structure sub-problems. In order to overcome this, we use a least-square stabilization method which was originally proposed in [10] for the elasticity problem. Here we adapt this approach to a general mixed displacement/velocity-pressure formulation on such hybrid meshes.

For simplicity, we only consider the following unified mixed displacement-pressure formulation (the extension to time dependent problems is straightforward): Find the displacement  $d$  and the pressure  $p$  such that

$$(5.11a) \quad -\nabla \cdot \varepsilon(d) + \nabla p = f \quad \text{in } \Omega,$$

$$(5.11b) \quad \nabla \cdot d + \vartheta p = 0 \quad \text{in } \Omega,$$

$$(5.11c) \quad d = 0 \quad \text{on } \Gamma,$$

where  $\Gamma = \partial\Omega$  denote the boundary of  $\Omega$ . The body force is prescribed by given functions  $f$ . In the limit case  $\vartheta = 0$ , we obtain the Stokes problem in a velocity-pressure mixed form.

**Remark 15.** For mixed Dirichlet and Neumann boundary conditions on pure tetrahedral or pure hexahedral meshes, we refer to [10]. An extension from the pure Dirichlet boundary conditions to the mixed boundary conditions and the Robin boundary conditions follows a similar procedure.

We approximate the displacement and the pressure by

$$(5.12) \quad V_h = [\tilde{V}_h]^3 \cap [C_0^1(\bar{\Omega})]^3 \quad \text{and} \quad Q_h = \tilde{V}_h \cap L_0^2(\Omega),$$

respectively, where  $L_0^2(\Omega) = \{q \in L^2(\Omega) : \int_{\Omega} q dx = 0\}$ . The discretized weak form for (5.11) reads: Find  $(d_h, p_h) \in V_h \times Q_h$  such that

$$(5.13) \quad \mathcal{B}(d_h, p_h; v, q) = \mathcal{F}(v, q)$$

for all  $(v, q) \in V_h \times Q_h$  with

$$\begin{aligned} \mathcal{B}(d, p; v, q) &= (\varepsilon(d), \varepsilon(v)) - (\nabla \cdot v, p) - (\nabla \cdot u, q) \\ &\quad - \vartheta(p, q) - \alpha \sum_M \sum_{T \subset M} h_T^2 (\nabla p, \nabla q)_T \end{aligned}$$

and

$$\mathcal{F}(v, q) = (f, v) - \alpha \sum_M \sum_{T \subset M} h_T^2 (f, \nabla q)_T,$$

where  $\alpha > 0$  is a stabilization constant.

We use some abbreviations for the norms:  $\|\cdot\|_0$  denotes  $\|\cdot\|_{L^2(\Omega)}$ ,  $\|\cdot\|_{0,T}$  denotes  $\|\cdot\|_{L^2(T)}$  and  $\|\cdot\|_1$  denotes  $\|\cdot\|_{H^1(\Omega)}$ .

For showing an optimal convergence rate of (5.13), let us first introduce the abbreviation for the seminorm

$$|q|_h = \left( \alpha \sum_M \sum_{T \subset M} h_T^2 \|\nabla q\|_T \right)^{1/2}.$$

A standard scaling arguments gives the following estimates:

$$(5.14) \quad |q|_h \leq c \|q\|_0, \quad \text{for all } q \in Q_h.$$

The boundedness of the bilinear form  $\mathcal{B}$  then follows from the above estimate (5.14) and the Schwarz inequality:

**Lemma 16.** *There is a positive constant  $c$  such that for all  $(d, p) \in V_h \times Q_h$  and  $(v, q) \in V_h \times Q_h$*

$$\mathcal{B}(d, p; v, q) \leq c (\|u\|_1^2 + (\varepsilon + 1) \|p\|_0^2)^{1/2} (\|v\|_1^2 + (\varepsilon + 1) \|q\|_0^2)^{1/2}$$

Using the argument of Verfürth's trick [18], we show the following stability inequality on hybrid meshes.

**Lemma 17.** *Assume that there exists a positive constant  $\underline{\alpha}$  such that for all elements the diameter  $h_T$  satisfies*

$$(5.15) \quad \underline{\alpha} h \leq h_T.$$

*Then, for the spaces  $V_h$  and  $Q_h$ , there exist positive constants  $c_1$  and  $c_2$  such that*

$$(5.16) \quad \sup_{0 \neq v \in V_h} \frac{(\nabla \cdot v, p)}{\|v\|_1} \geq c_1 \|p\|_0 - c_2 |p|_h,$$

*for all  $p \in Q_h$ .*

*Proof.* Due to the LBB condition on the continuous level, for  $p \in L_0^2(\Omega)$ , there exists a non-trivial  $w \in [H_0^1(\Omega)]^3$  such that

$$(5.17) \quad (\nabla \cdot w, p) \geq c_3 \|p\|_0 \|w\|_1$$

with some positive constant  $c_3$ .

Taking  $\tilde{w} = I_C w \in V_h \cap [H_0^1(\Omega)]^3$ , where the Clément operator  $I_C$  is defined in (5.8) for  $w$ , and by the estimates in Theorem 12, it is easy to see that

$$(5.18) \quad \|\tilde{w}\|_1 \leq c_4 \|w\|_1.$$

with a positive constant  $c_4$ . With the additional mesh assumption (5.15), we have an inverse estimate

$$(5.19) \quad \left( \sum_M \sum_{T \subset M} h_T^{-2} \|w - \tilde{w}\|_{0,T}^2 \right)^{1/2} \leq c_5 \|w\|_1,$$

where  $c_5$  is a positive constant.

Using the integration by parts on each  $T$ , the above interpolation estimate (5.18) and the Cauchy-Schwarz inequality, we obtain

$$\begin{aligned}
(\nabla \cdot \tilde{w}, p) &= (\nabla \cdot (\tilde{w} - w), p) + (\nabla \cdot w, p) \\
&\geq (\nabla \cdot (\tilde{w} - w), p) + c_3 \|w\|_1 \|p\|_0 \\
&= \sum_M \sum_{T \subset M} (w - \tilde{w}, \nabla p) + c_3 \|w\|_1 \|p\|_0 \\
&\geq - \left( \sum_M \sum_{T \subset M} h_T^{-2} \|w - \tilde{w}\|_{0,T}^2 \right)^{1/2} \left( \sum_M \sum_{T \subset M} h_T^2 \|\nabla p\|_{0,T}^2 \right)^{1/2} + c_3 \|w\|_1 \|p\|_0 \\
&\geq -c_5 \left( \sum_M \sum_{T \subset M} h_T^2 \|\nabla p\|_{0,T}^2 \right)^{1/2} \|w\|_1 + c_3 \|p\|_0 \|w\|_1 \\
&\geq -\frac{c_5}{c_4} \left( \sum_M \sum_{T \subset M} h_T^2 \|\nabla p\|_{0,T}^2 \right)^{1/2} \|\tilde{w}\|_1 + \frac{c_3}{c_4} \|p\|_0 \|\tilde{w}\|_1 \\
&\geq (c_7 \|p\|_0 - c_8 |p|_h) \|\tilde{w}\|_1
\end{aligned}$$

with positive constants  $c_7$  and  $c_8$ .

Finally, it is clear that, for  $0 \neq z \in V_h$ , we have

$$(5.20) \quad \left| \frac{(\nabla \cdot z, p)}{\|z\|_1} \right| \leq \frac{\|z\|_1 \|p\|_0}{\|z\|_1} = \|p\|_0.$$

We choose a fixed  $0 \neq z \in V_h$  and let  $v = \|\tilde{w}\|_1^{-1} \tilde{w} + \delta \|z\|_1^{-1} z$  and  $\delta > 0$ . Then if  $\delta < c_7$ , we have

$$\begin{aligned}
(\nabla \cdot v, p) &= \frac{(\nabla \cdot \tilde{w}, p)}{\|\tilde{w}\|_1} + \delta \frac{(\nabla \cdot z, p)}{\|z\|_1} \\
(5.21) \quad &\geq c_7 \|p\|_0 - c_8 |p|_h - \delta \|p\|_0 \\
&\geq c_9 \|p\|_0 - c_8 |p|_h,
\end{aligned}$$

where  $c_9 = c_7 - \delta > 0$ . Since  $\|v\|_1 \leq 1 + \delta$ , it follows that

$$(5.22) \quad \frac{(\nabla \cdot v, p)}{\|v\|_1} \geq \frac{1}{1 + \delta} (c_9 \|p\|_0 - c_8 |p|_h) = c_1 \|p\|_0 - c_2 |p|_h$$

with  $c_1 = \frac{c_9}{1 + \delta}$  and  $c_2 = \frac{c_8}{1 + \delta}$ . □

Using Lemma 17, then the following stability inequality follows.

**Theorem 18.** *There exists a positive constant  $c$  such that for all  $(d, p) \in V_h \times Q_h$  we have*

$$(5.23) \quad \sup_{(0,0) \neq (v,q) \in V_h \times Q_h} \frac{\mathcal{B}(d, p; v, q)}{(\|v\|_1^2 + (\vartheta + 1) \|q\|_0^2)^{1/2}} \geq c (\|d\|_1^2 + (\vartheta + 1) \|p\|_0^2)^{1/2}.$$

*Proof.* Let  $w \in V_h$  be chosen such that (5.16) is fulfilled and assume  $\|w\|_1 = \|p\|_0$ . Then using the bilinearity of  $\mathcal{B}$ , the Cauchy-Schwarz inequality, Lemma 17, and

the arithmetic-geometric-mean inequality, we obtain

$$\begin{aligned}
\mathcal{B}(d, p; w, 0) &= (\varepsilon(d), \varepsilon(w)) + (\nabla \cdot w, p) \\
&\geq -c_0 \|d\|_1 \|w\|_1 + (c_1 \|p\|_0 - c_2 |p|_h) \|w\|_1 \\
(5.24) \quad &= -c_0 \|d\|_1 \|p\|_0 + c_1 \|p\|_0^2 - c_2 \|p\|_0 |p|_h \\
&\geq -\frac{c_0}{2\gamma_1} \|d\|_1^2 + \left(c_1 - \frac{c_0\gamma_1}{2} - \frac{c_2\gamma_2}{2}\right) \|p\|_0^2 - \frac{c_2}{2\gamma_2} |p|_h^2 \\
&= -c_3 \|d\|_1^2 + c_4 \|p\|_0^2 - c_5 |p|_h^2
\end{aligned}$$

with positive constants  $c_i$ ,  $i = 0, \dots, 5$  and sufficiently small constants  $\gamma_1 > 0$ ,  $\gamma_2 > 0$ . Korn's inequality yields

$$\begin{aligned}
(5.25) \quad \mathcal{B}(d, p; d, -p) &= \|\varepsilon(d)\|_0^2 + \vartheta \|p\|_0^2 + |p|_h^2 \\
&\geq c_6 \|d\|_1^2 + \vartheta \|p\|_0^2 + |p|_h^2
\end{aligned}$$

with a positive constant  $c_6$ . Then choosing  $(v, q) = (d + \delta w, -p)$ ,  $0 < \delta < \min\{c_6/c_3, 1/c_5\}$ , and combining (5.24), (5.25) give

$$\begin{aligned}
(5.26) \quad \mathcal{B}(d, p; v, q) &= \mathcal{B}(d, p; d + \delta w, -p) \\
&= \mathcal{B}(d, p; d, -p) + \delta \mathcal{B}(d, p; w, 0) \\
&\geq (c_6 - \delta c_3) \|d\|_1^2 + (\delta c_4 + \vartheta) \|p\|_0^2 + (1 - \delta c_5) |p|_h^2 \\
&\geq c_7 (\|d\|_1^2 + (\vartheta + 1) \|p\|_0^2)
\end{aligned}$$

with a positive constant  $c_7$ .

On the other hand,

$$\begin{aligned}
(5.27) \quad \|v\|_1^2 + (\vartheta + 1) \|q\|_0^2 &= \|d + \delta w\|_1^2 + (\vartheta + 1) \|p\|_0^2 \\
&\leq 2\|d\|_1^2 + 2\delta^2 \|w\|_1^2 + (\vartheta + 1) \|p\|_0^2 \\
&= 2\|d\|_1^2 + (2\delta^2 + \vartheta + 1) \|p\|_0^2 \\
&\leq c_8 (\|d\|_1^2 + (\vartheta + 1) \|p\|_0^2)
\end{aligned}$$

with a positive constant  $c_8$ .

Combining (5.26) and (5.27) give (5.23) with  $c = c_7/2c_8$ .  $\square$

**5.4. An a priori error estimate.** The existence and uniqueness of the solution  $(d_h, p_h) \in V_h \times Q_h$  to the discrete problem (5.13) follows from Lemma 16 and Theorem 18.

Using the stability we have shown on hybrid meshes, applying the Lagrange interpolation as in Theorem 14 for  $d$  and the Clément interpolation as in Theorem 12 for  $p$ , and following the argument for the proof of Theorem 3.1 in [10], we arrive at the following a priori error estimate

**Theorem 19.** *Suppose that the solution to (5.11) satisfy  $d \in [H^2(\Omega)]^3$  and  $p \in H^1(\Omega)$ , then the discretization error estimate*

$$(5.28) \quad \|d - d_h\| + \|p - p_h\|_0 \leq ch(\|d\|_2 + \|p\|_1)$$

holds, with a positive constant  $c$ .

**Remark 20.** *If in addition, we have the regularity assumption*

$$\|d\|_2 + \|\varepsilon(d) - pI\|_1 \leq c\|f\|_0,$$

then using the Aubin-Nitsche trick, we have the following  $L^2$ -estimate for  $d$ ,

$$\|d - d_h\|_0 \leq C(h^2 \|d\|_2 + h \|p\|_1).$$

In [22], the original inf-sup stable MINI-element (see [6, 11]) on pure tetrahedral element has been extended to the Stokes problem on hybrid meshes by enlarging the piecewise linear velocity space on each hybrid element with a sufficient number of bubble functions. The stability is shown from an explicit construction of the so-called Fortin operator (see [6]). By applying static condensation, we eliminate the bubble functions, and arrive at a similar stabilized saddle point form as (5.13) which employs the least-square terms evaluated separately on each element.

**Remark 21.** *In addition, an instability may be caused by a dominating convection term in the fluid sub-problem. To resolve this, we follow the same approach used in [23].*

## 6. AMG METHODS FOR THE FLUID AND THE STRUCTURE SUB-PROBLEMS

**6.1. A generalized saddle point problem.** The saddle point system is given from the stabilized discretization (5.13) of sub-problems on hybrid meshes

$$(6.1) \quad K \begin{pmatrix} \underline{d} \\ \underline{p} \end{pmatrix} = \begin{pmatrix} \underline{f} \\ \underline{g}_h \end{pmatrix}$$

with

$$K = \begin{pmatrix} A & B^T \\ B & -C \end{pmatrix},$$

where  $A$  is symmetric and positive definite (SPD),  $B$  has full rank, and  $C$  is SPD (see Section 6.2). One easily sees that the (negative) Schur complement

$$S = BA^{-1}B^T + C$$

is SPD.

Here we use underline notations  $\underline{d}$  and  $\underline{p}$  indicating the vectors of the nodal degrees of freedom. The right hand side  $\underline{f}$  comes from the data and  $\underline{g}_h$  from the element-wise stabilization term  $-\alpha \sum_M \sum_{T \subset M} h_T^2 (f, \nabla q)$

**6.2. The AMG method for the saddle point problem.** For the saddle point system arising from the fluid sub-problem on pure tetrahedral mesh, a special AMG method which takes into account the stability property (the discrete inf-sup condition on coarse levels) has been studied by Markus Wabro (see [19, 20, 21]). In our previous work [22, 26], we extended the stabilized coarsening strategy to the discretized fluid problems on hybrid meshes.

In this paper, we consider the structure model in a displacement-pressure formulation, which eliminates the limitations from the pure displacement formulation and allows the Poisson ration  $\nu \rightarrow 0.5$ . Thus it fits into the original saddle point problem for the fluid sub-problem with a little modification of the  $C$  block in (6.1):

$$(6.2) \quad c(p, q) = \vartheta(p, q) + \alpha \sum_M \sum_{T \subset M} h_T^2 (\nabla p, \nabla q)$$

for all  $p, q \in Q_h$  (for the Stokes problem  $\vartheta = 0$ ), or in a matrix-vector representation

$$(6.3) \quad \underline{p}C\underline{q} = \vartheta\underline{p}M_c\underline{q} + \alpha\underline{p}C_c\underline{q},$$

where  $\underline{p}$  and  $\underline{q}$  are vectors of the degrees of freedom corresponding to the finite element functions  $p$  and  $q$ , respectively,  $M_C$  is the scalar mass matrix, and  $C_c$  denotes the scalar Laplace matrix scaled with the discretization parameter  $h_T$ .

**Remark 22.** *Since the variational problem in pure displacement formulation for the compressible linear elasticity model on the structure domain is symmetric and coercive, this leads to linear systems with SPD matrices. AMG methods for solving such problems are well-studied, see, e.g., [16] for scalar differential equations and [12] for an extension to systems of partial differential equations in a natural block-wise fashion (block-wise interpolation). The special AMG method used in our experiments is taken from the work of [14], which was originally developed for discrete elliptic second-order problems and was extended to the structure problem on hybrid meshes in a straightforward way, see [26, 22, 23]. However, as is well known, in the limiting case when the Poisson ratio  $\nu \rightarrow 0.5$ , the stiffness matrix from pure displacement becomes ill-conditioned. Thus the AMG methods mentioned above will lose their optimality under such a situation unless it is not modified properly.*

The AMG method for the saddle point systems requires an appropriate coarsening strategy and a smoothing procedure.

6.2.1. *The stabilized coarsening strategy.* In order to avoid a mixture of the displacement/velocity and pressure unknowns on coarse levels, we construct the prolongation operator from the coarse level  $l+1$  to the next finer level  $l$  in a block-diagonal matrix form:

$$(6.4) \quad P_{l+1}^l : \begin{pmatrix} (\mathbb{R}^3)^{m_{l+1}} \\ \mathbb{R}^{m_{l+1}} \end{pmatrix} \longrightarrow \begin{pmatrix} (\mathbb{R}^3)^{m_l} \\ \mathbb{R}^{m_l} \end{pmatrix},$$

$$P_{l+1}^l = \begin{pmatrix} I_{l+1}^l & \\ & J_{l+1}^l \end{pmatrix},$$

where  $m_l$  is the number of pressure (or one component of displacement/velocity) degrees of freedom on the level  $l$ ,  $I_{l+1}^l$  and  $J_{l+1}^l$  are prolongation matrices for the displacement/velocity and pressure, respectively.

For the restriction from the finer level  $l$  to the next coarser level  $l+1$  we choose the transposed matrix:

$$R_l^{l+1} = (P_{l+1}^l)^T = \begin{pmatrix} I_l^{l+1} & \\ & J_l^{l+1} \end{pmatrix},$$

where  $I_l^{l+1} = (I_{l+1}^l)^T$  and  $J_l^{l+1} = (J_{l+1}^l)^T$ . The system matrix on the level  $l$  is denoted by  $K_l$  with a form

$$K_l = \begin{pmatrix} A_l & B_l^T \\ B_l & -C_l \end{pmatrix}.$$

The system matrix on the next coarser level  $l+1$  is obtained by the Galerkin projection method:

$$K_{l+1} = R_l^{l+1} K_l P_{l+1}^l = \begin{pmatrix} A_{l+1} & B_{l+1}^T \\ B_{l+1} & -C_{l+1} \end{pmatrix}$$

with  $A_{l+1} = I_l^{l+1} A_l I_{l+1}^l$ ,  $B_{l+1} = J_l^{l+1} B_l I_{l+1}^l$ , and

$$(6.5) \quad C_{l+1} = \vartheta(M_c)_{l+1} + \alpha \frac{\lambda_{\max}(D_l^{-1} M_l)}{h^2} (C_c)_{l+1},$$

where  $M_l$  is the vector mass matrix obtained by Galerkin projection on level  $l$ ,  $(M_c)_{l+1}$  the scalar mass matrix obtained by Galerkin projection on level  $l+1$ ,  $D_l$  the diagonal of  $A_l$ , and  $(C_c)_{l+1}$  the scaled Laplace matrix obtained by Galerkin projection on level  $l+1$ . Since the matrix  $C_c$  involves mesh-dependent stabilization parameters, the standard Galerkin projection may cause a loss of stability on coarse levels. Therefore, a remedy has been applied for coarsening the matrix  $C_c$ .

Then using the same strategy as in [22], under appropriate assumptions on the hybrid mesh, we obtain the following stability results on all coarse levels

**Theorem 23.** *For each coarse level  $l = \{2, \dots, L\}$ , there is a positive constant  $\zeta_l$  such that*

$$(6.6) \quad \sup_{0 \neq (\underline{v}, \underline{q}) \in \underline{V}_l \times \underline{Q}_l} \frac{\underline{B}_l((\underline{u}, \underline{p}), (\underline{v}, \underline{q}))}{\|\underline{v}\|_{A_l} + (1 + \vartheta)\|\underline{q}\|_{M_l}} \geq \zeta_l (\|\underline{u}\|_{A_l} + (1 + \vartheta)\|\underline{p}\|_{M_l})$$

for all  $(\underline{u}, \underline{p}) \in \underline{V}_l \times \underline{Q}_l = (\mathbb{R}^3)^{m_l} \times \mathbb{R}^{n_l}$ , where

$$\underline{B}_l((\underline{u}, \underline{p}), (\underline{v}, \underline{q})) = \underline{v}^T A_l \underline{u} + \underline{v}^T B_l^T \underline{p} + \underline{q}^T B_l \underline{u} - \underline{q}^T C_l \underline{p}.$$

We remark that for a level  $l$ ,  $l \in \{2, \dots, L\}$

$$(6.7) \quad \underline{V}_l := (\mathbb{R}^3)^{m_l}, \quad \underline{Q}_l := \mathbb{R}^{n_l},$$

are the spaces of the coefficient vectors corresponding to the following finite element spaces on level  $l > 1$

$$\begin{aligned} V_l &= \{v \in V_h : \exists \underline{v}_l \in \underline{V}_l \text{ such that } \underline{v} = I_2^1 I_3^2 \dots I_l^{l-1} \underline{v}_l\}, \\ Q_l &= \{p \in Q_h : \exists \underline{q}_l \in \underline{Q}_l \text{ such that } \underline{p} = J_2^1 J_3^2 \dots J_l^{l-1} \underline{q}_l\}, \end{aligned}$$

respectively, where  $n_l$  denote the numbers of unknowns for one component of the displacement/velocity or for the pressure on the level  $l$ .

We note that in case  $\vartheta = 0$ , we obtain the stability on coarse levels for the Stokes problem, which was presented in [26] and shown in [22].

**6.2.2. The smoothing procedure.** A Braess-Sarazin-type smoother was used as smoothing procedure, which was originally introduced in [5] and has a smoothing property with a rate of  $\mathcal{O}(1/m)$ , where  $m$  is the number of smoothing steps.

One step of the smoothing procedure consists of applications of the inexact Uzawa algorithm:

$$\begin{aligned} \hat{A}(\hat{u}^{k+1} - u^k) &= f - Au^k - B^T p^k, \\ \hat{S}(p^{k+1} - p^k) &= B\hat{u}^{k+1} - Cp^k - g, \\ \hat{A}(u^{k+1} - u^k) &= -B^T(p^{k+1} - p^k), \end{aligned}$$

which correspond to a preconditioned Richardson method:

$$\begin{pmatrix} u^{k+1} \\ p^{k+1} \end{pmatrix} = \begin{pmatrix} u^k \\ p^k \end{pmatrix} + \hat{K}^{-1} \begin{pmatrix} f - Au^k - B^T p^k \\ g - Bu^k + Cp^k \end{pmatrix}$$

with a symmetric and indefinite preconditioner

$$\hat{K} = \begin{pmatrix} \hat{A} & B^T \\ B & \hat{A}^{-1} B^T - \hat{S} \end{pmatrix},$$

where  $\hat{A}$  and  $\hat{S}$  are SPD preconditioners for  $A$  and the (negative) inexact Schur complement  $C + B\hat{A}^{-1}B^T$ , respectively.

As suggested in [19], we use  $\hat{A} = 2D$  (a damped Jacobi iteration), where  $D$  denotes the diagonal of  $A$ . The choice  $\hat{S} = C + B^T \hat{A}^{-1} B$  corresponds to the original Braess-Sarazin smoother. It requires the (exact) solution of the equation

$$(C + B^T \hat{A}^{-1} B)(p^{k+1} - p^k) = B\hat{u}^{k+1} - Cp^k - g.$$

We use instead one step of an (inner) AMG method with starting value 0 to solve this equation approximately. See [27] for an analysis of such an approximate Braess-Sarazin smoother.

## 7. NUMERICAL EXPERIMENTATIONS

### 7.1. The setup of numerical experimentations.

*7.1.1. Computational domain, material parameters, boundary and initial conditions.* All the following numerical experiments are performed on a straight cylinder vessel, which is quite often used, see e.g., [26, 7, 8]. The fluid domain is a cylinder in the  $z$ -direction of length 50 mm and radius 5 mm. The thickness of the surrounding structure is 1 mm.

The structure medium is a linear Saint Venant-Kirchhoff material with the density  $\rho^s = 1.2 \text{ g/cm}^3$  and the Young's modulus  $E = 2.9908e + 06 \text{ dyn/cm}^2$ . The Poisson ration will be set according to our specified numerical tests. The fluid medium has the density  $\rho^f = 1.0 \text{ g/cm}^3$  and the viscosity  $\mu = 0.03 \text{ poise}$ .

For the fluid, we set the Neumann data  $g_{in} = (0, 0, 1.332 \times 10^4)^T \text{ dyn/cm}^2$  on the inlet for time  $t \leq 3 \text{ ms}$  and  $g_{in} = 0 \text{ dyn/cm}^2$  afterwards. The structure and the fluid are initially at rest.

*7.1.2. Hybrid meshes and their conforming subdivisions.* Hybrid meshes are generated for the fluid and the structure domains with matching nodes at the common interface (see [13]). Two meshes are used for simulations, see Table. 4. The coarse

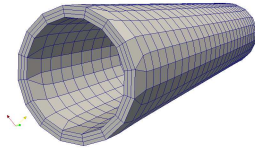
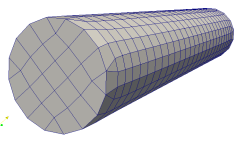
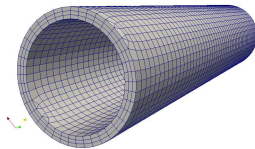
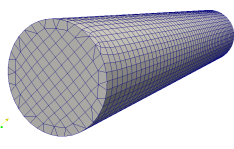
1,944 structure elements	2,021 fluid elements
	
7,434 structure elements	10,055 fluid elements
	

TABLE 4. Two hybrid meshes for the FSI computational domain.

hybrid mesh contains 4,176 nodes and 3,965 elements (1,944 structure elements

and 2,021 fluid elements), and the fine hybrid mesh contains 17,904 nodes and 17,489 elements (7,434 structure elements and 10,055 fluid elements). The overall degrees of freedom for these two meshes are about 16,000 and 70,000, respectively.

For the first finite element method, we need to make a conforming subdivision of each hybrid mesh without adding new nodes. The resulting coarse tetrahedral mesh includes 22,474 elements (11,520 structure elements and 10,954 fluid elements), and the resulting fine tetrahedral mesh includes 98,158 elements (44,388 structure elements and 53,770 fluid elements). See Table 5.

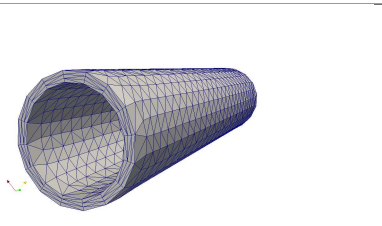
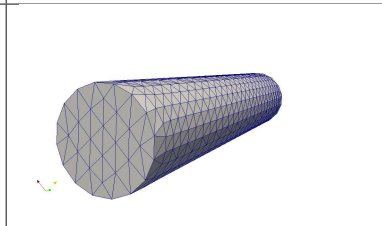
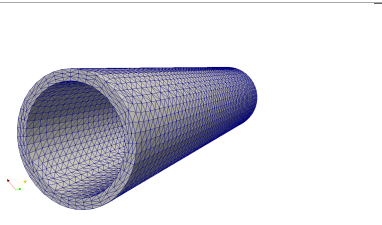
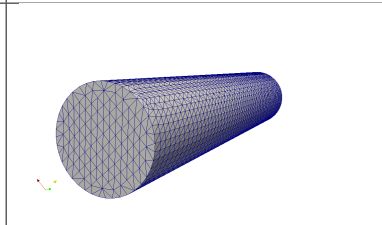
11,520 structure elements	10,954 fluid elements
	
44,388 structure elements	53,770 fluid elements
	

TABLE 5. Two tetrahedral meshes subdivided from the hybrid meshes.

**Remark 24.** *Note in principle, that it is not required to generate the subdivision in an explicit way for both finite element methods. The finite element assembly is performed element-wise on the original hybrid mesh, with special care of the corresponding subdivision of each non-tetrahedral element.*

**7.2. Numerical solutions with compressible and nearly incompressible materials.** In this Subsection, we present some numerical solutions with a compressible material and several nearly incompressible materials.

7.2.1. *A compressible case.* For  $E = 2.9908e + 06$  dyn/cm<sup>2</sup>,  $\nu = 0.3003$ , by the following relations for the Lamé constants

$$\lambda^l = \frac{E\nu}{(1+\nu)(1-2\nu)} \text{ and } \mu^l = \frac{E}{2(1+\nu)},$$

we obtain  $\mu^l = 1.15 \times 10^6$  dyn/cm<sup>2</sup> and  $\lambda^l = 1.73 \times 10^6$  dyn/cm<sup>2</sup>. In this case, the numerical results of the FSI problem with pure displacement formulation were reported in [23, 26]. Here we use the same material parameters and compare the numerical solutions of mixed displacement-pressure formulation with the solutions of the pure displacement formulation in [23, 26].

In Table 6, we compare the fluid pressure wave propagations along the center line of the cylinder using the pure displacement and mixed displacement-pressure

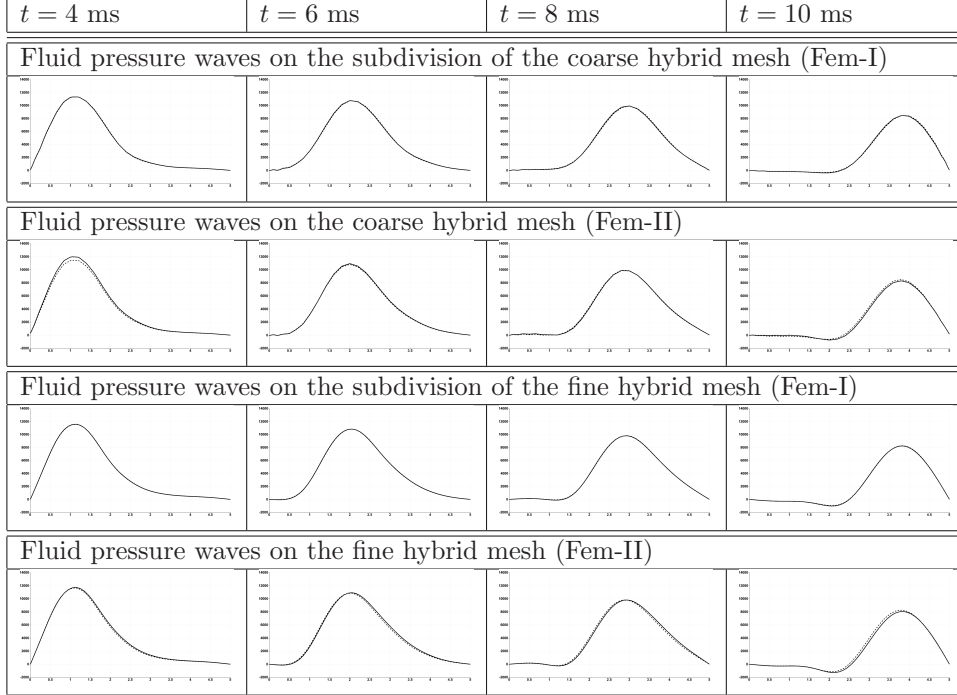


TABLE 6. Numerical comparisons of the fluid pressure wave propagations with pure displacement and mixed displacement-pressure formulations.

formations. For a comparison, we use a time step size  $\delta t = 0.125$  ms, and plot the fluid pressure waves at time levels  $t \in \{4, 6, 8, 10\}$  ms. The fluid pressure waves from the pure displacement formulation are indicated by the dash lines, the fluid pressure waves from the mixed formulation are indicated by the solid lines. The horizontal axis represents the center line of the cylinder; the fluid pressure is plotted in the vertical direction. We compare these waves obtained from the two finite element discretizations discussed in Section 5.

From the comparison in Table 6, we observe the convergence of the numerical solutions using the two finite element discretizations on the coarse and the fine meshes. It is also easy to see that the numerical solutions with the mixed formulation reproduce the solutions with the pure displacement formulation when the material is compressible  $\nu \ll 0.5$ .

Moreover, we will see in the following some numerical results obtained from the FSI problem with the mixed displacement-pressure formulation in the case  $\nu \rightarrow 0.5$ .

7.2.2. *Nearly incompressible cases.* In order to compare the numerical solutions of the mixed formulation using different choices of the Poisson ratio when it goes to limit, i.e.,

$$\nu \in \mathcal{W} := \{0.49, 0.4999, 0.499999, 0.49999999\},$$

we test the FSI algorithms on the hybrid mesh with time step size  $\Delta t = 0.125$  ms. See the fluid pressure waves along the center line at time levels  $t \in \{4, 6, 8, 10\}$  ms

in Table 7. In addition, we present the structure pressure wave along the line with a starting point  $(0, 5.5, 0)$  mm and an ending point  $(0, 5.5, 50)$  mm in Table 8.

The numerical solutions with different  $\nu \in \mathcal{W}$  are indicated by the solid lines, the dash lines, the dot lines, and the dash dot lines, respectively. The horizontal axis represents the center line of the cylinder; the fluid pressure is plotted in the vertical direction.

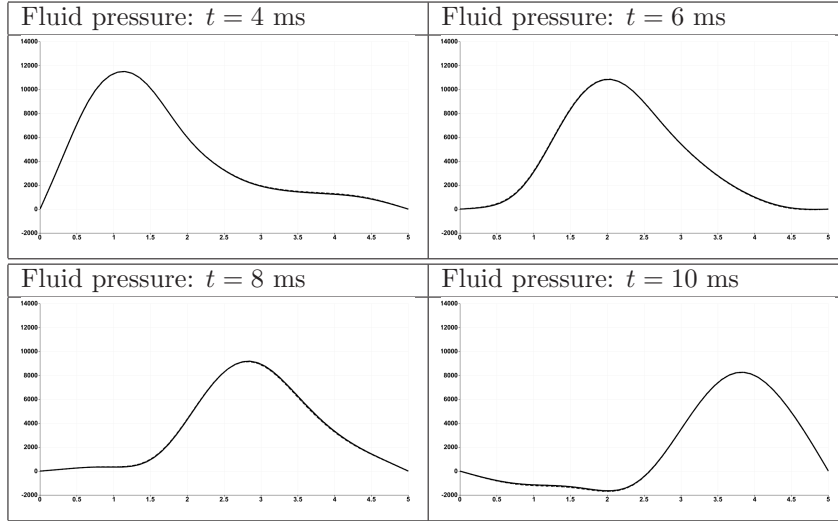


TABLE 7. The propagation of fluid pressure waves obtained using nearly incompressible mixed formulations.

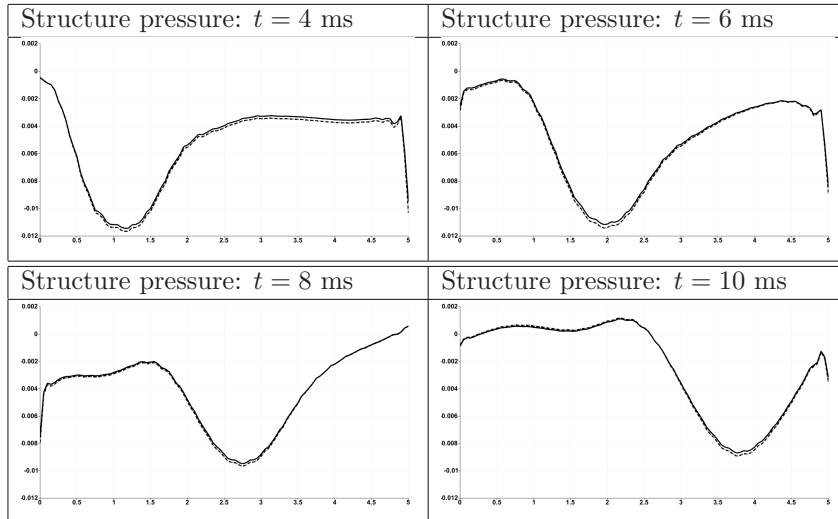


TABLE 8. The propagation of structure pressure waves obtained using nearly incompressible mixed formulations.

It is obvious that for each time level, the waves are conforming well to each other in the limit case when  $\nu \rightarrow 0.5$ . Hence our numerical methods are stable for the Poisson ratio  $\nu \rightarrow 0.5$ .

7.2.3. *A comparison of a nearly incompressible case  $\nu = 0.49999999$  and a compressible case  $\nu = 0.303$ .* We also compare the fluid pressure waves (see Table 9) along the center line and the structure pressure waves (see Table 10) along the line starting at  $(0, 5.5, 0)$  mm and ending at  $(0, 5.5, 50)$  mm, using  $\nu = 0.49999999$  and  $\nu = 0.303$ . We use a time step size  $\Delta t = 0.125$  ms. The numerical solutions with  $\nu = 0.49999999$  and  $\nu = 0.303$  are indicated by the solid lines, and the dash lines, respectively. The horizontal axis represents the center line of the cylinder; the fluid pressure is plotted in the vertical direction.

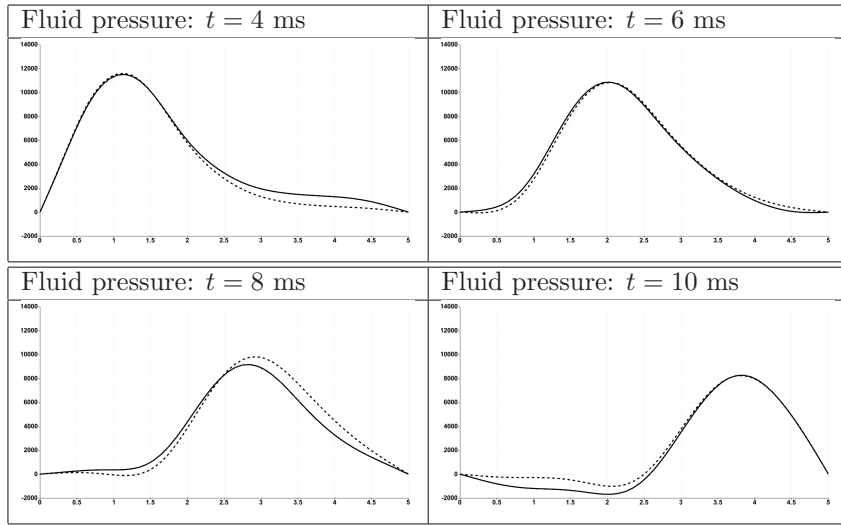


TABLE 9. The comparison of the fluid pressure wave propagation with a nearly incompressible material  $\nu = 0.49999999$  and a compressible material  $\nu = 0.303$ .

It is easy to see that in this situation, for the compressible and the nearly incompressible materials, the fluid pressure waves, as well as the structure pressure waves behave slightly differently from each other. However, we still observe reasonable results.

7.2.4. *A comparison of numerical solutions with different time step size  $\Delta t = \{0.25, 0.125, 0.0625\}$  ms.* In [26, 23], we compared in detail the numerical solutions using different time step sizes, with the pure displacement formulation. For the mixed displacement-pressure formulation, we compare the fluid pressure waves along the center line on the fine hybrid mesh for the case  $\nu = 0.499999$ . We use time the step size  $\Delta t = \{0.25, 0.125, 0.0625\}$  ms. See the numerical solutions in Table 11, where the pressure waves with different time step size  $\Delta t = \{0.25, 0.125, 0.0625\}$  ms are indicated by the dash dot lines, the dash lines and the solid lines, respectively. The horizontal axis represents the center line of the cylinder; the fluid pressure is plotted in the vertical direction.

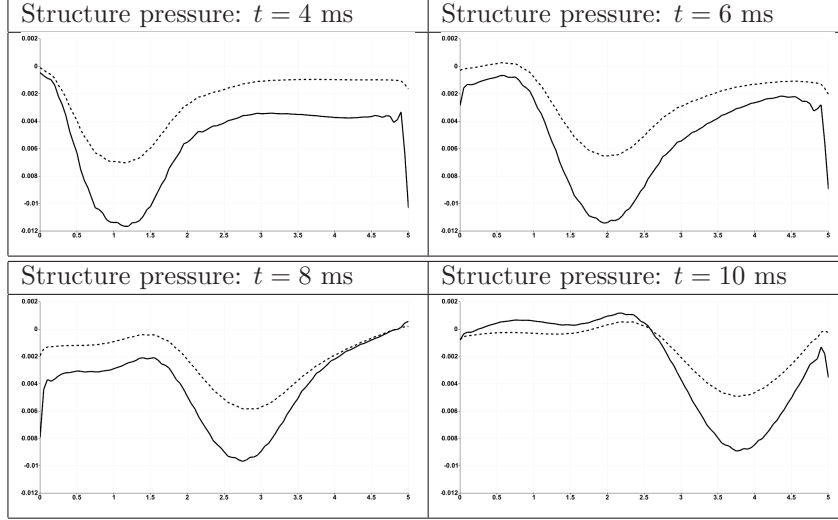


TABLE 10. The comparison of the structure pressure wave propagation with a nearly incompressible material  $\nu = 0.4999999$  and a compressible material  $\nu = 0.303$ .

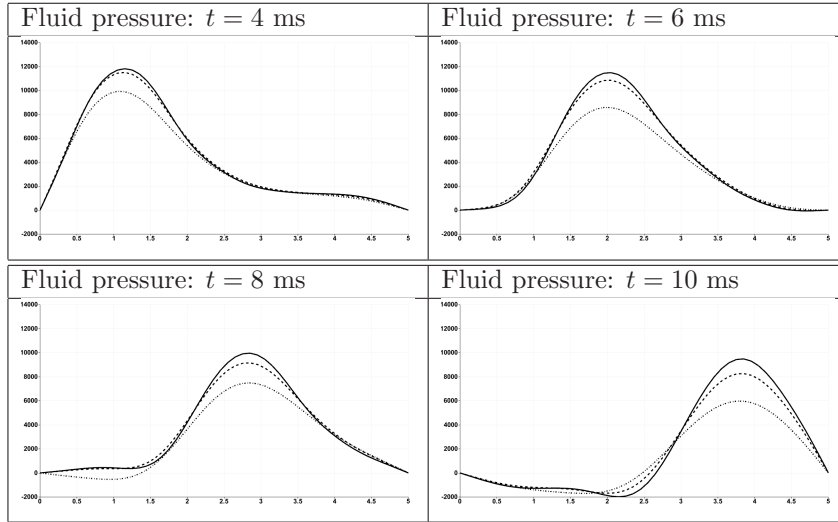


TABLE 11. The comparison of the fluid pressure wave propagations with a nearly incompressible material  $\nu = 0.499999$  using different time step size  $\Delta t = \{0.25, 0.125, 0.0625\}$  ms.

It is obvious that, our numerical solutions obtained from the mixed displacement-pressure formulations are convergent with respect to the time step size, in the limit case when  $\nu \rightarrow 0.5$ . For the structure pressure waves, we observe a similar convergence behavior with respect to time step size  $\Delta t$ .

**Remark 25.** For all the above numerical tests, we observe very similar numerical results obtained from the preconditioned GMRES solver and the Newton solver performed on the FSI system with two finite element discretizations on different meshes.

**7.3. Performance.** For measuring the performance, we test the FSI solvers (RN preconditioned GMRES and Newton) on a laptop with an Intel Core of 2.67 GHz and 4 GB memory. We fix the Poisson ratio  $\nu = 0.499999$ , set the relative residual error reduction by a factor  $1e - 05$ , and choose the time step size  $\Delta t \in \{0.0625, 0.125, 0.25\}$  ms.

FSI solvers		Preconditioned GMRES							
Meshes		Coarse				Fine			
FEMs		Fem-I		Fem-II		Fem-I		Fem-II	
Cost	#It	Time	#It	Time	#It	Time	#It	Time	
0.0625 ms	8	294 s	8	386 s	8	1179 s	8	3757 s	
0.125 ms	5	337 s	5	445 s	4	1103 s	4	3747 s	
0.25 ms	6	621 s	6	751 s	6	2007 s	6	4576 s	

FSI solvers		Newton							
Meshes		Coarse				Fine			
FEMs		Fem-I		Fem-II		Fem-I		Fem-II	
Cost	#It	Time	#It	Time	#It	Time	#It	Time	
0.0625 ms	2	2649 s	2	3001 s	2	14913 s	3	80887 s	
0.125 ms	3	5848 s	3	6377s	3	28967 s	3	86993 s	
0.25 ms	3	8862 s	3	8787 s	3	35667 s	3	92066 s	

TABLE 12. Comparison of cost for solving the FSI problem at one time step using two FSI solvers and two finite element discretizations (FEMs: Fem-I and Fem-II) on hybrid meshes.

See the iteration numbers and cost (measured in seconds (s)) in Table 12. As expected, the first finite element method (Fem-I) is more efficient than the second one (Fem-II) for all these test cases due to its faster finite element assembly procedure. For comparing the performance of the the RN preconditioned GMRES solver and the Newton based solver, we use the same relative residual error reduction factor  $1e - 06$  as the stopping criteria. For each finite element method, the RN preconditioned GMRES solver is more efficient than the Newton based solver.

The AMG performance for the fluid sub-problem, and for the structure sub-problem in the pure displacement formulation has been reported in [23]. Here we present the AMG performance for the structure sub-problem in the mixed displacement-pressure formulation. We need to solve the structure sub-problems with Dirichlet and Neumann boundary conditions on the interface, respectively. For the Dirichlet problem, we set the residual reduction by a factor around  $1e - 08$ . Since the Neumann problem is used as a preconditioner, we solve the the problem with the residual error reduction factor up to  $1e - 03$ . The iteration numbers and the time in seconds (s) are listed in Table 13.

We observe in Table 13, that the iteration numbers stay in the same range for the Dirichlet problem. For the Neumann problem, we observe decreasing iteration

FEMs	Fem-I on the coarse mesh				Fem-II on the coarse mesh			
Interface	Dirichlet		Neumann		Dirichlet		Neumann	
Cost	#It	Time	#It	Time	#It	Time	#It	Time
0.0625 ms	9	24 s	9	24 s	7	22 s	6	19 s
0.125 ms	12	32 s	20	54 s	9	29 s	14	45 s
0.25 ms	13	34 s	37	98 s	10	32 s	34	109 s

---

FEMs	Fem-I on the fine mesh				Fem-II on the fine mesh			
Interface	Dirichlet		Neumann		Dirichlet		Neumann	
Cost	#It	Time	#It	Time	#It	Time	#It	Time
0.0625 ms	7	79 s	7	79 s	5	66 s	4	53 s
0.125 ms	9	101 s	13	145 s	7	93 s	10	133 s
0.25 ms	10	111 s	26	290 s	7	92 s	17	224 s

TABLE 13. Comparison of the AMG cost for the mixed displacement-pressure formulation using two finite element discretizations (FEMs: Fem-I and Fem-II) on hybrid meshes, with different boundary conditions on the interface, and with different time step size.

numbers with respect to the decreasing time step size since small time step size improves the nice property for the almost-pure Neumann matrices (with very little Dirichlet conditions on two ends of the structure vessel). It is also easy to see the CPU time of the AMG solver is scaled well with respect to the iteration numbers and the problem size.

For  $\nu \rightarrow 0.5$ , we observe very similar performance of the iteration numbers and the cost.

## 8. CONCLUSIONS

In this work, we extend our previous developed FSI solvers for a pure displacement elasticity formulation to a more general mixed displacement-pressure one, which is able to handle the nearly incompressible elasticity material. The RR (RN) iteration has been reinterpreted by introducing two Lagrangian multipliers. We also developed the stabilized piecewise linear finite element discretization on a general hybrid mesh for such a nearly incompressible model. A robust AMG solver with respect to the Poisson ratio for such a saddle point problem on hybrid meshes has been developed.

## ACKNOWLEDGEMENTS

The author would like to thank Prof. Ulrich Langer for fruitful discussions on smoothing this paper.

## REFERENCES

- [1] R. A. Adams and J. J. F. Fournier. *Sobolev Spaces*, volume 140 of *Pure and Applied Mathematics*. Academic Press, Amsterdam, Boston, second edition, 2003.
- [2] S. Badia, F. Nobile, and C. Vergara. Fluid-structure partitioned procedures based on Robin transmission conditions. *Journal of Computational Physics*, 227:7027–7051, 2008.
- [3] S. Badia, F. Nobile, and C. Vergara. Robin-Robin preconditioned Krylov methods for fluid-structure interaction problems. *Comput. Methods Appl. Mech. Engrg.*, 198:1768–2784, 2009.

- [4] D. Braess. *Finite Elements. Theory, fast solvers, and applications in solid mechanics*. Springer, Berlin, Heidelberg, New York, 2nd edition, 2001.
- [5] D. Braess and R. Sarazin. An efficient smoother for the Stokes problem. *Appl. Numer. Math.*, 23:3–19, 1997.
- [6] F. Brezzi and M. Fortin. *Mixed and Hybrid Finite Element Methods*. Springer series in computational mathematics. Springer, New York, 1991.
- [7] S. Deparis, M. Discacciati, G. Fourestey, and A. Quarteroni. Fluid-structure algorithms based on Steklov-Poincaré operators. *Comput. Methods Appl. Mech. Engrg.*, 195:5797–5812, 2006.
- [8] M. A. Fernández and M. Moubachir. A Newton method using exact Jacobians for solving fluid-structure coupling. *Comput. & Struct.*, 83(2-3):127–142, 2005.
- [9] L. Formaggia and F. Nobile. A stability analysis for the arbitrary Lagrangian Eulerian formulation with finite elements. *East-West Journal of Numerical Mathematics*, 7:105–132, 1999.
- [10] Leopoldo P. Franca and R. Stenberg. Error analysis of some Galerkin least square methods for the elasticity equations. *SIAM Journal on Numerical Analysis*, 28(6):1680–1697, 1991.
- [11] V. Girault and P.A. Raviart. *Finite Element Methods for Navier-Stokes Equations: Theory and Algorithms*. Springer, New York, 1985.
- [12] M. Griebel, D. Oeltz, and M. A. Schweitzer. An algebraic multigrid method for linear elasticity. *SIAM. J. Sci. Comput.*, 25:385–407, 2003.
- [13] F. Kicking. Website. <http://www.meshing.org/>.
- [14] F. Kicking. Algebraic multigrid for discrete elliptic second-order problems. In *Multigrid Methods V. Proceedings of the 5th European Multigrid conference (ed. by W. Hackbush), Lecture Notes in Computational Sciences and Engineering, vol. 3*, pages 157–172. Springer, 1998.
- [15] U. Langer, H. Yang, and W. Zulehner. Numerical simulation of fluid-structure interaction problems on the grid environment. In J. Volkert, T. Fahringer, D. Kranzlmüller, R. Kobler, and W. Schreiner, editors, *Proceedings of 3rd Austria Grid Symposium*, pages 13–27. OCG publisher, Vienna, 2010.
- [16] J. W. Ruge and K. Stüben. Algebraische mehrgittermethodenalgebraic multigrid (AMG). In *Multigrid Methods*, volume 3 of *Frontiers in Applied Mathematics*, pages 73–130. SIAM, Philadelphia, 1987.
- [17] Y. Saad and M. H. Schultz. Gmres : A generalized minimal residual algorithm for solving nonsymmetric linear system. *SIAM J. Sci. Stat. Comput.*, 7:856–869, 1986.
- [18] R. Verfürth. Error estimates for a mixed finite element approximation of the Stokes equations. *R.A.I.R.O. Num. Anal.*, 18(2):175–182, 1984.
- [19] M. Wabro. *Algebraic Multigrid Methods for the Numerical Solution of the Incompressible Navier-Stokes Equations*. PhD thesis, Johannes Kepler University Linz, 2003.
- [20] M. Wabro. Coupled algebraic multigrid methods for the oseen problem. *Comput. Vis. Sci.*, 7:141–151, 2004.
- [21] M. Wabro. AMG<sub>e</sub>—coarsening strategies and application to the Oseen equations. *SIAM J. Sci. Comput.*, 27:2077–2097, 2006.
- [22] H. Yang. *Numerical Simulation of Fluid-Structure Interaction Problems on Hybrid Meshes with Algebraic Multigrid Methods*. PhD thesis, Johannes Kepler University Linz, 2010. available online <http://www.numa.uni-linz.ac.at/Teaching/PhD/Finished/huidongyang>.
- [23] H. Yang. A Numerical Study on a Preconditioned GMRES Solver with Algebraic Multigrid Accelerations for the Fluid-Structure Interaction Problems on Hybrid Meshes. Technical Report 2011-15, Johann Radon Institute for Computational and Applied Mathematics (RICAM), 2011. submitted, available online <http://www.ricam.oeaw.ac.at/publications/reports/11/rep11-15.pdf>.
- [24] H. Yang. Two finite element methods on hybrid meshes and their applications to the fluid-structure interaction problems. Technical Report 2011-24, Johann Radon Institute for Computational and Applied Mathematics (RICAM), 2011. submitted, available online <http://www.ricam.oeaw.ac.at/publications/reports/11/rep11-24.pdf>.
- [25] H. Yang and W. Zulehner. A Newton based fluid-structure interaction solver with algebraic multigrid methods on hybrid meshes. In Y. Huang, R. Kornhuber, O. Widlund, and J. Xu, editors, *Domain Decomposition Methods in Science and Engineering*, pages 285–292. Springer, 2011.

- [26] H. Yang and W. Zulehner. Numerical simulation of fluid-structure interaction problems on hybrid meshes with algebraic multigrid methods. *Journal of Computational and Applied Mathematics*, 235:5367–5379, 2011.
- [27] W. Zulehner. A class of smoothers for saddle point problems. *Computing*, 65:227–246, 2000.

JOHANN RADON INSTITUTE FOR COMPUTATIONAL AND APPLIED MATHEMATICS, AUSTRIAN ACADEMY OF SCIENCES, ALTENBERGERSTRASSE 69, A-4040 LINZ, AUSTRIA, TEL.: +43 (0) 732 2468 5256

*E-mail address:* `huidong.yang@oeaw.ac.at`